Master thesis

Shape coexistence and superdeformation in ^{28}Si

Inter-University Master Degree on Nuclear Physics

Author:
Dorian Grzegorz Frycz

Advisors:
Javier Menéndez Sánchez & Antonio Márquez Romero

UNIVERSITAT DE BARCELONA

July 2023

Acknowledgements

I would like to express my gratitude towards my advisors Javier Menéndez Sánchez, Antonio Márquez Romero and Arnau Ríos Huguet for their invaluable support and guidance throughout the whole research as well as their meticulous review of this Master thesis, which I am truly proud of the outcome. The knowledge and skills I have gained under their supervision are truly priceless. Furthermore, I would like to express my heartfelt gratitude to the new friends I have made during this time. Lastly, I am deeply thankful to my family and long-standing friends for their unwavering support and encouragement in all aspects of my life.

Contents

Abstract

In this Master thesis I analyze the ^{28}Si nucleus within the nuclear shell model using state-of-the-art numerical diagonalizations complemented with the generator-coordinate method (GCM) with quadrupole-constrained Hartree-Fock-Bogoliubov (HFB) wavefunctions. Experimentally, ^{28}Si presents shape coexistence between the oblate ground state and an excited prolate structure with bandhead at 6.7 MeV. Although the standard USDB interaction, which is very successful in describing the nuclear structure of nuclei in this mass region, reproduces well the oblate ground state, it fails at establishing a prolate band. Therefore, a modification of the USDB interaction must be introduced to reproduce the experimental spectrum. Guided by analytical Elliot's SU(3) scheme, I show that this is achieved by slightly lowering the gap between the nearly degenerate $1d_{5/2}$-$2s_{1/2}$ doublet and the $1d_{3/2}$ orbital. My calculations suggest that the oblate ground state is mostly 0p-0h configurations in the $1d_{5/2}$-$2s_{1/2}$ orbitals, whereas the prolate band consists mainly of 4p-4h excitations into the $1d_{3/2}$ orbital.

Additionally, I study whether ^{28}Si can exhibit a superdeformed structure at higher energies. In order to achieve such deformations, excitations from the *sd* to the *pf* shell must be taken into account. I find that most of the deformation contribution comes from the $1f_{7/2}$-$2p_{3/2}$ doublet and that the most favorable states are prolate 2p-2h and 4p-4h excitations into the *pf* shell. In contrast to previous studies, my numerical calculations suggest that this superdeformed structure would mix with normal-deformed configurations, and therefore ^{28}Si would not present a superdeformed band.

1. Introduction to deformation in nuclei

The strong interaction among protons and neutrons allows the existence of self-bound systems known as atomic nuclei. As a result of the intricate characteristics of the strong interaction, collective phenomena emerge, wherein nucleons cooperate to exhibit behaviors such as rotations or vibrations centered around a specific intrinsic shape. Apart from the spherical shape, atomic nuclei can exhibit axially symmetric quadrupole deformations, including prolate shapes, which are axially symmetric spheroids elongated along one axis, and oblate shapes, which are flattened. Furthermore, atomic nuclei can manifest triaxial deformations, in which elongation takes place along distinct axes, resulting in an intermediate shape that presents additional complexity.

Across the nuclear chart, an abundance of ground states exhibit quadrupole deformations, which originate from the quadrupole-quadrupole interactions of the nucleons. Among these deformations, axially symmetric shapes and prolate configurations stand out as the most common shapes. However, the scenario becomes even more complex as multiple states with distinct intrinsic shapes can coexist within the same nucleus, occupying a narrow energy range of a few MeV. The occurrence of this phenomenon, known as shape coexistence, has been observed across various regions of the nuclear chart [1], indicating its widespread presence. Hitherto, medium-mass nuclei, including ^{32}S [2], ^{36}Ar [3], ^{40}Ar [4], ^{40}Ca [5], ^{42}Ca [6], and ^{44}Ti [7] have been identified as examples where competition between spherical and various types of deformed states occurs. For instance, the ^{40}Ca nucleus is as a doubly magic nucleus with a spherical ground state. However, Fig. 1.1 shows that at an excitation energy of $\sim$3 MeV, a prolate normal deformed shape emerges, and at $\sim$5 MeV it presents a prolate superdeformed shape [8], which is of particular interest due to its extreme deformation. This superdeformed states have been studied in numerous nuclei such as ^{24}Mg [9], ^{28}Si [10, 11], ^{32}S [12], and ^{40}Ar [13, 14].

In this work, I explore the nuclear structure of ^{28}Si, an even-even nucleus composed of 14 protons and 14 neutrons, which exhibits the phenomenon of shape coexistence between oblate and prolate deformations. Previous studies [15, 16] have shown that the three lowest-energy 0^+ states are bandheads of an oblate rotational band, a vibrational band of the oblate ground state and a prolate rotational band, as shown in Fig. 1.1. These rotational bands are manifestations of a permanent intrinsic deformation, shared among the states that belong to the band, each of which is labeled by its total angular momentum number, J. Therefore, ^{28}Si demonstrates shape coexistence between prolate and oblate states, while the spherical state does not persist, in contrast with the prediction of the spherical mean field of Mayer and Jensen [17, 18]. In addition, there have been recent attempts at finding a superdeformed band in ^{28}Si [19], predicted by a theoretical calculation [16].

The objective of this study is to gain insight into the nuclear structure of ^{28}Si by employing both simple analytical models such as SU(3) as well as state-of-the-art numerical shell model calculations that shed light on its shape coexistence.

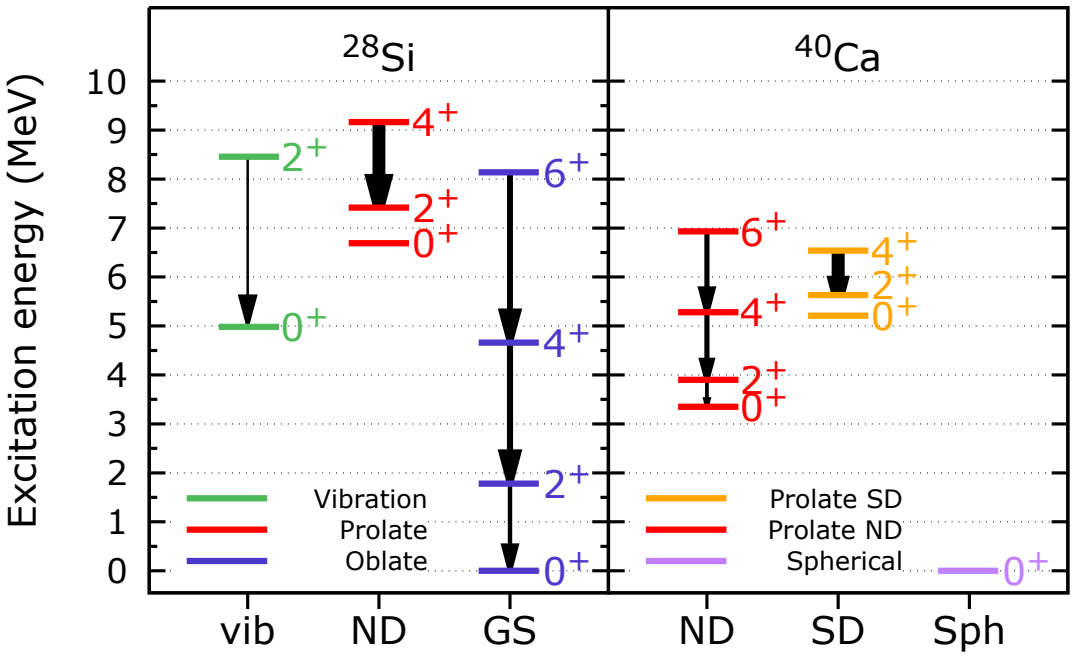

Figure 1.1: Experimental data of the band structure of ^{28}Si, from [15], and ^{40}Ca, from [5]. The ^{28}Si nucleus exhibits an oblate rotational band and its vibration as well as a prolate rotational band. On the other hand, ^{40}Ca presents a spherical ground state and two prolate rotational bands: one with normal deformation and another one that is superdeformed. The arrows' width indicate the $B(E2)$ transition strength between states of a particular band. Outband transitions and other low-energy states are not shown for clarity.

1.1 Collective models

An atomic nucleus in a deformed state can exhibit collective rotational or vibrational motion, which can be discerned by a characteristic energy spectrum.

In order to understand collective motion in nuclei, two frames of reference are required: the laboratory frame and the intrinsic frame. For axially symmetric shapes, the quantum number associated to the projection of the total angular momentum ($\vec{J}$) in the laboratory frame is denoted as M while in the intrinsic frame it is K, as represented in Fig. 1.2.

Rotational motion is exclusive to permanently deformed nuclei, as any rotation around a symmetry axis leaves the surface invariant, except for an insignificant global phase in the wavefunction [20]. In consequence, spherical shapes are invariant under any rotation and axially-symmetric nuclei are invariant under rotations around their symmetry axis. A straightforward approach to modeling the rotations of a deformed nucleus is to treat it as an ideal rigid rotor [20] characterized by a constant moment of inertia, denoted as $\mathcal{I}$. The Hamiltonian of an axially-symmetric rotor about a principal axis, denoted as 3 in the intrinsic frame of reference, is

$$\mathcal{H}_{\text{rot}} = \frac{(\vec{J}_1^2 + \vec{J}_2^2)}{2\mathcal{I}} = \frac{(\vec{J}^2 - \vec{J}_3^2)}{2\mathcal{I}}, \tag{1.1}$$

where $\vec{J}_i$ are the components of the total angular momentum $\vec{J}$. By quantizing the values of the total angular momentum and its projection on the symmetry axis we

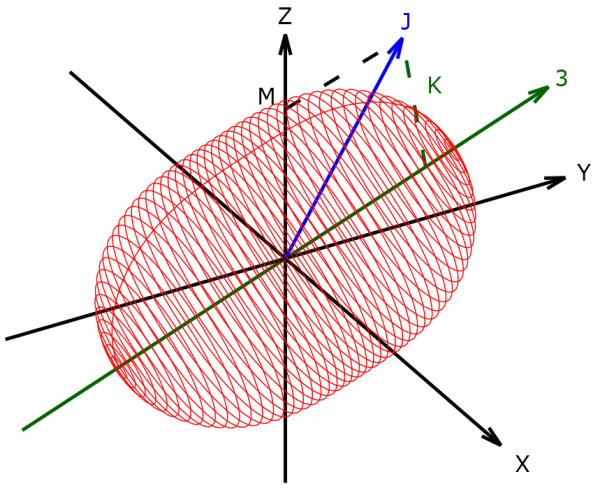

Figure 1.2: Projections of the total angular momentum ($\vec{J}$) of a prolate spheroid on the laboratory frame of reference (M), defined by the {X,Y,Z} axes, and on the intrinsic frame of reference (K), where the symmetry axis is labeled as 3.

end up with the expression

$$E_{\text{rot}} = \frac{J(J+1) - K^2}{2\mathcal{I}}, \tag{1.2}$$

where J is the total angular momentum number and natural units are employed ($\hbar = 1$). The energy levels exhibit a proportionality to $J(J+1)$, manifesting a distinct pattern that can be readily identified in the spectrum. This succession of levels with energies proportional to $J(J+1)$ that share a permanent deformation is called a rotational band. The values of angular momentum J are dependent on their projection along the symmetry axis K such as

$$K \neq 0 \rightarrow J = K, K+1, K+2...; \; M = -J, ..., J \; ; \tag{1.3}$$

$$K = 0 \rightarrow J = 0, 2, 4...; \; M = -J, ..., J \; , \tag{1.4}$$

where the $K = 0$ case only admits even values of J due to axial symmetry [20]. This sequence of levels that are spaced out by the $E \propto J(J+1)$ proportionality provides a strong indication of the presence of deformation in a nucleus.

1.2 Quadrupole moment and deformation parameters

The interaction between the nucleus and the electromagnetic field yields valuable information regarding the nuclear properties. By employing gamma radiation, it is possible to excite the nucleus to higher energy levels, and analyzing the characteristics of the emitted radiation can offer valuable insight into its structure.

The surface of a nucleus can be described in terms of the spherical harmonics

$Y_{\lambda\mu}(\theta,\varphi)$ [20]:

$$R(\theta,\varphi) = R_0\left[1+\sum_{\lambda=0}^{\infty}\sum_{\mu=-\lambda}^{\lambda}\alpha_{\lambda\mu}Y_{\lambda\mu}(\theta,\varphi)\right], \tag{1.5}$$

where R_0 is the radius of the spherical nucleus, (r,θ,φ) are the spherical coordinates and $\alpha_{\lambda\mu}$ are the expansion coefficients. In the context of nuclear excitations, the monopole term ($\lambda = 0$) corresponds to a change of the nuclear volume, which necessitates a significant amount of energy due to the high incompressibility of nuclear matter. On the other hand, the dipole term ($\lambda = 1$) describes a shift of the center of mass, which is an insignificant translation. The remaining terms represent different deformations of the nucleus, although modes with $\lambda \geq 5$ are generally negligible. The most common types of deformation across the nuclear chart are the quadrupole deformations ($\lambda = 2$).

The distribution of the electric charge in a nucleus can be described by the electromagnetic multipole moments

$$Q_{\lambda\mu} = r^{\lambda}Y_{\lambda\mu}(\theta,\varphi). \tag{1.6}$$

We can also define its hermitian average operator as [21]

$$\overline{Q}_{\lambda\mu} = \frac{1}{2}\left[Q_{\lambda\mu} + (-1)^{\mu}Q_{\lambda-\mu}\right]. \tag{1.7}$$

For quadrupole deformations, there are three relevant quadrupole moments $\overline{Q}_{20}$, $\overline{Q}_{21}$ and $\overline{Q}_{22}$. With these operators, we can define a set of dimensionless quadrupole deformation parameters (β,γ) that characterize an arbitrary triaxial shape

$$\beta = \frac{4\pi}{3R_0^2Ab^2}\sqrt{\langle\overline{Q}_{20}\rangle^2 + 2\langle\overline{Q}_{22}\rangle^2}, \tag{1.8}$$

$$\gamma = \arctan\left(\frac{\sqrt{2}\langle\overline{Q}_{22}\rangle}{\langle\overline{Q}_{20}\rangle}\right), \tag{1.9}$$

with the nucleus mean radius $R_0 \simeq 1.2A^{1/3}$ fm and $\langle O\rangle \equiv \langle\Psi|O|\Psi\rangle$ indicates the mean value of an operator for a given nucleus state $|\Psi\rangle$. The harmonic oscillator parameter b can be derived using the expression [22]

$$b = \sqrt{\frac{\hbar}{m_N\omega}} = \sqrt{\frac{\hbar}{m_N\omega}}\cdot\frac{\sqrt{\hbar}c}{\sqrt{\hbar}\sqrt{c^2}} = \frac{\hbar c}{\sqrt{(m_Nc^2)(\hbar\omega)}} \simeq \frac{197.33\ \text{MeVfm}}{\sqrt{938.9\ \text{MeV}\cdot\hbar\omega}}, \tag{1.10}$$

where $\hbar$ represents Planck's reduced constant, c denotes the speed of light, ω represents the angular frequency of the harmonic oscillator, and m_N corresponds to the mass of a nucleon. By utilizing the Blomqvist–Molinari formula [23], $\hbar\omega = (45A^{-1/3} - 25A^{-2/3})$ MeV, and simplifying the constants as 41.4 MeV fm^2 , we can arrive at the standard parametrization

$$b^2 \simeq 41.4/(45A^{-1/3} - 25A^{-2/3})\ \text{fm}^2 \tag{1.11}$$

for the harmonic oscillator parameter.

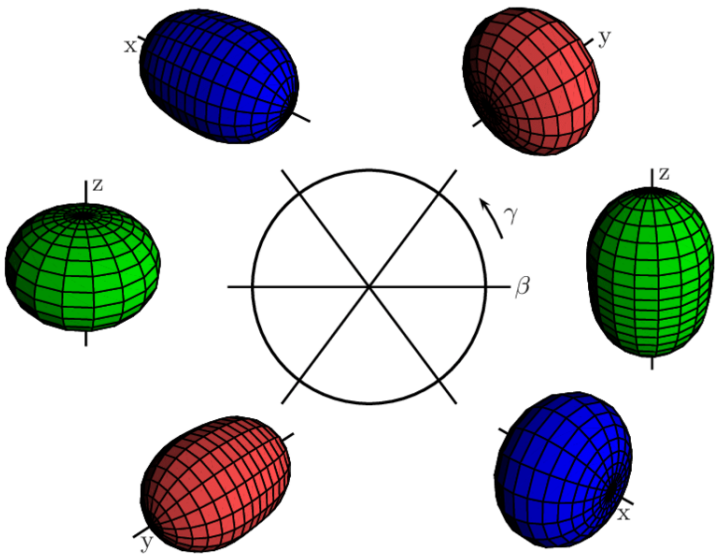

Figure 1.3: Hill-Wheeler coordinates (β, γ) for the representation of quadrupole deformations. Oblate and prolate shapes are represented with principal axes along the z-axis (green), y-axis (red) and x-axis (blue). Figure extracted from [24].

Revisiting the set of deformation parameters (β, γ), the parameter β quantifies the magnitude of deformation in a nucleus, which can be related to the axis ratio of spheroid shapes. In normal deformed states (ND), typical values fall within the range of $0.2 \leq \beta \leq 0.3$, corresponding to an axis ratio of 3:2. On the other hand, superdeformed states (SD) exhibit $\beta \geq 0.5$, resulting in a 2:1 axis ratio.

The parameter γ characterizes the type of deformation. Initially, γ can assume values between 0° and 360°. However, considering that Q_{21} determines only the orientation of the shape in space, it can be set to $Q_{21} = 0$, narrowing down the interval to $0° \leq \gamma \leq 60°$ as illustrated in Fig. 1.3. A value of $\gamma = 0°$ corresponds to a prolate shape, while $\gamma = 60°$ represents an oblate shape. Any other value of γ within this range indicates a triaxial deformation. In the case of axially symmetric shapes, it is standard to simplify the description by using only the parameter β. The differentiation between prolate and oblate shapes is then determined by the sign of β. Positive values indicate a prolate shape, while negative values indicate an oblate shape. This two shapes are for instance represented in green in Fig. 1.3, taking z as the symmetry axis.

Using the set of quadrupole deformation parameters (β, γ), we can establish an intrinsic shape for the nucleus. However, we still need a method to connect this intrinsic description with the experimental data in the laboratory frame of reference.

The electric quadrupole moment provides a measure of the nucleus' deformation, as it characterizes the deviation of the charge distribution from a spherical shape. In the case of spherical shapes, the quadrupole moment vanishes. In the laboratory frame, a microscopic description of the quadrupole moment is [22]

$$Q_{\text{spec}} \equiv \sqrt{\frac{16\pi}{5}} \sqrt{\frac{J(2J-1)}{(J+1)(2J+1)(2J+3)}} (J||Q_2||J), \tag{1.12}$$

where $Q_2 = \sum_{j=1}^{A} e_j r_j^2 Y_{20}(\theta_j, \varphi_j)$: e_j are the effective nuclear charges of the nucleons

and A is the mass number. The expression features the $(J||Q_2||J)$ reduced matrix element, which does not depend on the projection of the angular momentum M according to the Wigner-Eckart theorem [25]. In fact, this definition of Q_{spec} matches the classical limit for the intrinsic quadrupole moment Q_0, which is related to the spectroscopy one by [26]

$$Q_{0,s} = \frac{(J+1)(2J+3)}{3K^2 - J(J+1)} Q_{spec}(J), \text{ with } K \neq 1. \tag{1.13}$$

Positive intrinsic quadrupole moments indicate prolate shapes while negative ones represent oblate shapes. For a $K = 0$ rotational band, Eq. (1.13) simplifies to

$$Q_{0,s} = \frac{-(2J+3)}{J} Q_{spec}(J). \tag{1.14}$$

Another way to quantify the quadrupole moment comes from the reduced $B(E2)$ transition strength between an initial (J_i) and a final (J_f) state, which are greatly enhanced within a rotational band:

$$B(E2; J_i \to J_f) \equiv \frac{1}{2J_i + 1} |(J_i||Q_2||J_f)|^2. \tag{1.15}$$

We can extract the intrinsic quadrupole moment [8] from these transitions as

$$Q_{0,t} = \pm \sqrt{\frac{16\pi B(E2, J \to J-2)}{5|\langle J200|J-2, 0\rangle|^2}}, \tag{1.16}$$

where $\langle J200|J-2, 0\rangle$ is a Clebsch-Gordan coefficient with the $\langle j_1 j_2 m_1 m_2|JM\rangle$ notation. Both the $B(E2)$ and Q_{spec} are measurable observables that provide insight on the intrinsic shape of the nucleus, as indicated by Eqs. (1.13) and (1.16). For a rotational band associated with a well-established permanently deformed shape, the intrinsic quadrupole moments fulfill $Q_{0,s} \approx Q_{0,t}$.

2. Theoretical framework

2.1 Spherical mean field

Describing atomic nuclei is challenging. Fundamentally, the nucleus is a self-bound system composed of strongly-interacting nucleons, protons (Z) and neutrons (N). However, the intricacies of the strong force at low energies are poorly known from first principles due to the non-perturbative nature of Quantum Chromodynamics (QCD) in the typical nuclear scale, with Fermi momenta of $\simeq 200$ MeV. Moreover, the inherent complexities of solving many-body systems necessitate the implementation of approximate methods. Therefore, in the case of a non-relativistic system comprising A nucleons with two-body interactions, the many-body problem can be formulated using the following Hamiltonian

$$\mathcal{H} = \sum_{i}^{A} t_i + \sum_{i,j}^{A} V_{ij}, \tag{2.1}$$

where t_i is the kinetic energy operator and V_{ij} is the two-body interaction. Although three-body forces are not taken into account explicitly, it is possible to include their effects indirectly through density-dependent or normal-ordering terms in the one-body and two-body interaction interaction [27].

The subsequent task involves solving the time-independent Schrödinger equation

$$\mathcal{H}|\Psi\rangle = E|\Psi\rangle, \tag{2.2}$$

which entails determining the eigenvectors and eigenenergies of the system. However, numerous challenges arise from this seemingly straightforward problem. Firstly, the description of the nucleus considering explicitly all nucleons interacting through realistic interactions, known as *ab initio* or first-principles methods, is only possible for light nuclei [28, 29] and selected heavier systems [30, 31]. For instance, Quantum Monte Carlo (QMC) techniques are limited to $A \leq 12$ [32] and no-core shell model (NCSM) to $A \leq 22$ [33, 34], only with the selection of the most relevant configurations. Thus, approximate methods are required to treat medium and heavy-mass nuclei.

A commonly employed approach is to assume that the particles move independently within the average potential generated by all other nucleons (v_i). This method, known as the mean-field approximation, significantly simplifies the problem by reducing it to finding solutions for a particle moving within a potential

$$h_i|\phi_i\rangle = (t_i + v_i)|\phi_i\rangle = \epsilon_i|\phi_i\rangle, \tag{2.3}$$

where h_i is the single-particle Hamiltonian, $|\phi_i\rangle$ are the single-particle levels and ϵ_i are the single-particle energies. Throughout the years, the spherical harmonic

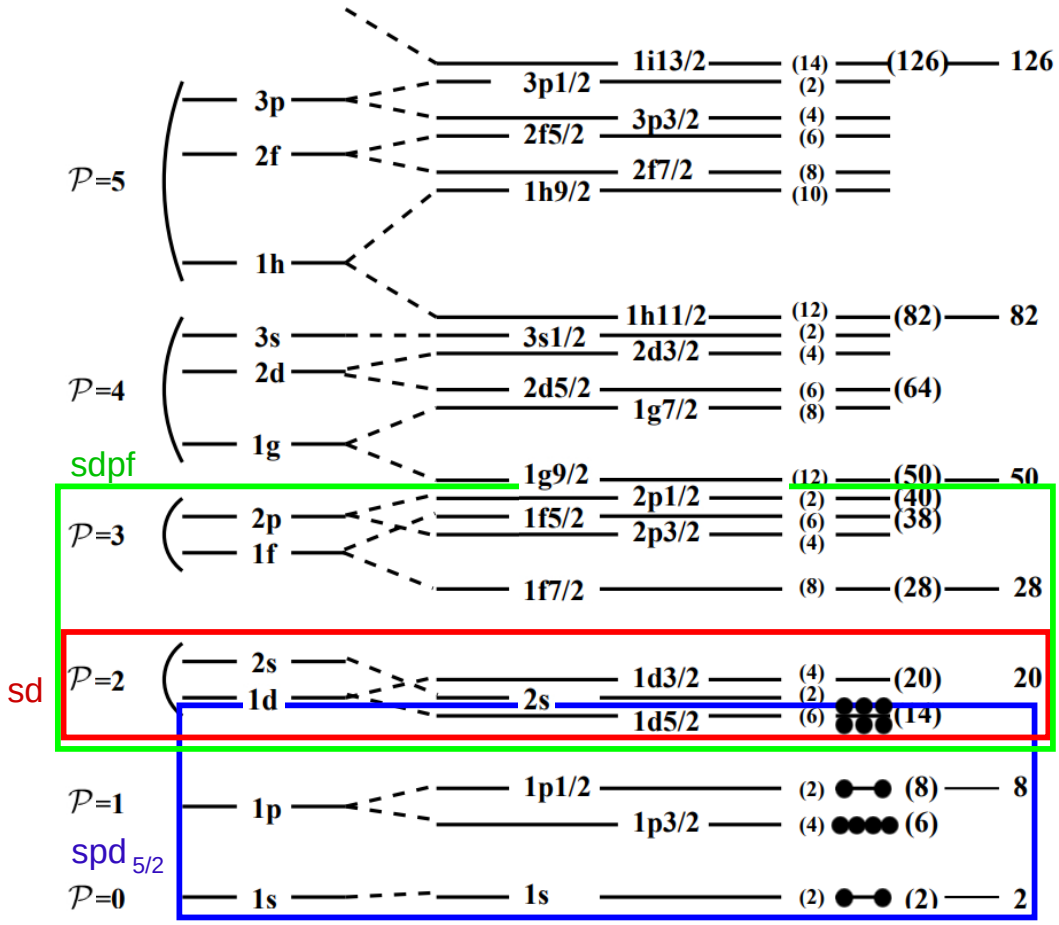

Figure 2.1: Single-particle states of the spherical harmonic oscillator with spin-orbit term. The black circles represent the filling for ^{28}Si ground state in the spherical mean field. Different valence spaces used throughout the work are highlighted: *sd* shell in red, *sdpf* in green and $spd_{5/2}$ in blue. Figure modified from [26].

oscillator has demonstrated its reliability as a suitable choice for the mean-field description. Its numerous symmetries enable the assignment of states with well-defined quantum numbers. However, it is crucial to supplement this choice with a robust spin-orbit term, denoted as v_{LS}, to accurately reproduce experimental observations such as the presence of magic numbers [17]. Then, the spherical mean-field potential is

$$v = v_{\text{H.O.}} + v_{\text{orb}} + v_{LS} = \frac{1}{2}m\omega^2\vec{r}^{\,2} + A\vec{l}^{\,2} + B\vec{l}\cdot\vec{s}, \tag{2.4}$$

where ω is the angular frequency, $\vec{l}$ is the orbital angular momentum, $\vec{s}$ is the spin and A and B are constants. The major oscillator shells are labeled with the principal number $\mathcal{P}$ and their energies are $\epsilon_{\mathcal{P}} = (\mathcal{P}+\frac{3}{2})\hbar\omega$ with degeneracy $D = (\mathcal{P}+1)(\mathcal{P}+2)$. Next, they are split by their values of the orbital angular momentum number l, since $\langle lm|\vec{l}^2|lm\rangle = l(l+1)$. Finally, the orbits are labeled with the quantum numbers $|nlj\rangle$, for neutrons and protons, with degeneracy $D = 2j+1$ due to the spin-orbit term, where n is the radial quantum number. Figure 2.1 shows the final single-particle states of the spherical harmonic oscillator.

In summary, we have simplified the challenging task of solving a complex Hamil-

tonian $\mathcal{H}$ for the many-body problem to one that is, in principle, readily solvable $\mathcal{H}_0 = \sum_i h_i$. The many-body wavefunction $|\Phi_{\text{Slater}}\rangle$ is derived by filling the single-particles levels with A particles, a Slater determinant, and the energy is calculated as the sum of their individual energies

$$|\Phi_{\text{Slater}}\rangle = \frac{1}{\sqrt{A!}}\det\left\{\prod_i^A |\phi_i\rangle\right\}, \tag{2.5}$$

$$E = \sum_i^A \epsilon_i. \tag{2.6}$$

This Slater determinant can be written in a more convenient way using the second quantization formalism:

$$|\Phi_{\text{Slater}}\rangle = \prod_i^A c_i^\dagger|-\rangle, \tag{2.7}$$

where $c_i^\dagger$ are the creation operators and $|-\rangle$ is its bare vacuum.

According to this simple picture, for ^{28}Si, the spherical mean-field orbits should be filled up to the $1d_{5/2}$ orbit, inclusive, with 14 protons and 14 neutrons, as shown in Fig. 2.1. Therefore, the ground state wavefunction is represented by a single Slater determinant, resulting in a spherical shape. However, experimental data reveals that ^{28}Si is an oblate nucleus, and calls for a more complex formalism.

2.2 Analytical SU(3) scheme

Elliot's SU(3) model [35] offers a straightforward explanation of the deformation of atomic nuclei. The model begins with the assumption of a one-body spherical harmonic oscillator potential. However, to simplify the calculations, three approximations are made. Firstly, the consideration is limited to a single major harmonic oscillator shell $\mathcal{P}$. Secondly, the energy levels associated with the orbits within this major shell are assumed to be degenerate, as the spin-orbit coupling is neglected. Lastly, the interactions between particles are restricted to two-body quadrupole-quadrupole interactions, which are actually one of the main components of the nuclear force [36]. The spherical harmonic oscillator Hamiltonian (with $m = 1$ and $\omega = 1$) is

$$\mathcal{H}_0 = T + V = \frac{1}{2}(\vec{p}^{\,2} + \vec{r}^{\,2}) = \frac{1}{2}(\vec{p} + i\vec{r})(\vec{p} - i\vec{r}) + \frac{3}{2}\hbar = \left(\vec{A}^\dagger\vec{A} + \frac{3}{2}\right), \tag{2.8}$$

where $\vec{A} = (\vec{p}+i\vec{r})/\sqrt{2}$ and $\vec{p}$ is the linear momentum. These complex vectors belong to the symmetry group U(3), which has nine generators. From the antisymmetric combinations we recover the three components of the orbital angular momentum vectors L_x, L_y and L_z. The six symmetric bi-linears are reduced to five because the trace, the mean field energy, is constant. This is the reason why the relevant group is SU(3) instead of U(3). Then the five remaining generators are the components of the quadrupole operator

$$q_\mu^{(2)} = \frac{\sqrt{6}}{2\hbar}\left((\vec{p}\times\vec{p})_\mu^{(2)} + (\vec{r}\times\vec{r})_\mu^{(2)}\right). \tag{2.9}$$

For a system of $\mathcal{N}$ particles in a major harmonic oscillator shell the total quadrupole moment and angular orbital moment are

$$Q_\mu^{(2)} = \sum_{i=1}^{\mathcal{N}} q_{\mu,i}^{(2)}, \tag{2.10}$$

$$\vec{L} = \sum_{i=1}^{\mathcal{N}} \vec{l}_i, \tag{2.11}$$

and the Casimir operator of SU(3), which is the operator that commutes with every generator of the group, is introduced as

$$C_{\mathrm{SU(3)}} = \frac{3}{4}(\vec{L}\cdot\vec{L}) + \frac{1}{4}(Q_\mu^{(2)}\cdot Q_\mu^{(2)}). \tag{2.12}$$

The Casimir operator eigenvalues can be determined as

$$C_{\mathrm{SU(3)}}(\lambda,\mu) = \lambda^2 + \lambda\mu + 3(\lambda+\mu) \tag{2.13}$$

and they are expressed in terms of the usual SU(3) irreducible representations (λ,μ), which are related to the cartesian quantum numbers of the harmonic oscillator by $n_x = n_y + \mu$, $n_z = n_y + \lambda + \mu$ and $3n_y + \lambda + 2\mu = \mathcal{N}\mathcal{P}$.

Then, the Hamiltonian

$$\mathcal{H} = \mathcal{H}_0 + \chi(Q^{(2)}\cdot Q^{(2)}), \tag{2.14}$$

can be rewritten as

$$\mathcal{H} = \mathcal{H}_0 + 4\chi C_{\mathrm{SU(3)}} - 3\chi(\vec{L}\cdot\vec{L}). \tag{2.15}$$

The eigenenergies of this Hamiltonian are finally

$$E = \hbar\omega\left(\mathcal{P} + \frac{3}{2}\right) + 4\chi\left[\lambda^2 + \lambda\mu + 3(\lambda+\mu)\right] - 3\chi L(L+1). \tag{2.16}$$

In atomic nuclei, the quadrupole interactions among nucleons are attractive ($\chi < 0$) and they tend to be significant. As a result, the ground state of a nucleus corresponds to the representation (λ,μ) that maximizes the intrinsic quadrupole moment of the nucleus, as shown in Eq. (2.14). The formation of rotational bands is a natural consequence of this, where states within a given (λ,μ) representation, which determines the deformation, follow a sequence with energies proportional to $L(L+1)$. If spin is included this $L(L+1)$ dependence changes to a $J(J+1)$ one, coupling orbital angular momentum to spin $\vec{J} = \vec{L} + \vec{S}$.

With the SU(3) formalism, one can make a new prediction for ^{28}Si. In this context, the task at hand involves identifying the configuration that maximizes the quadrupole moment. To maximize the quadrupole moment, we examine the distribution of 6 neutrons and 6 protons within the *sd* shell, which corresponds to the $\mathcal{P} = 2$ major harmonic oscillator shell (orbitals inside the red box in Fig 2.1). Diagram 2.2 a) provides a way to calculate the Q_0 value within the SU(3) model. Each level exhibits a fourfold degeneracy in quadruple moment contribution, arising from the combination of spin and isospin.

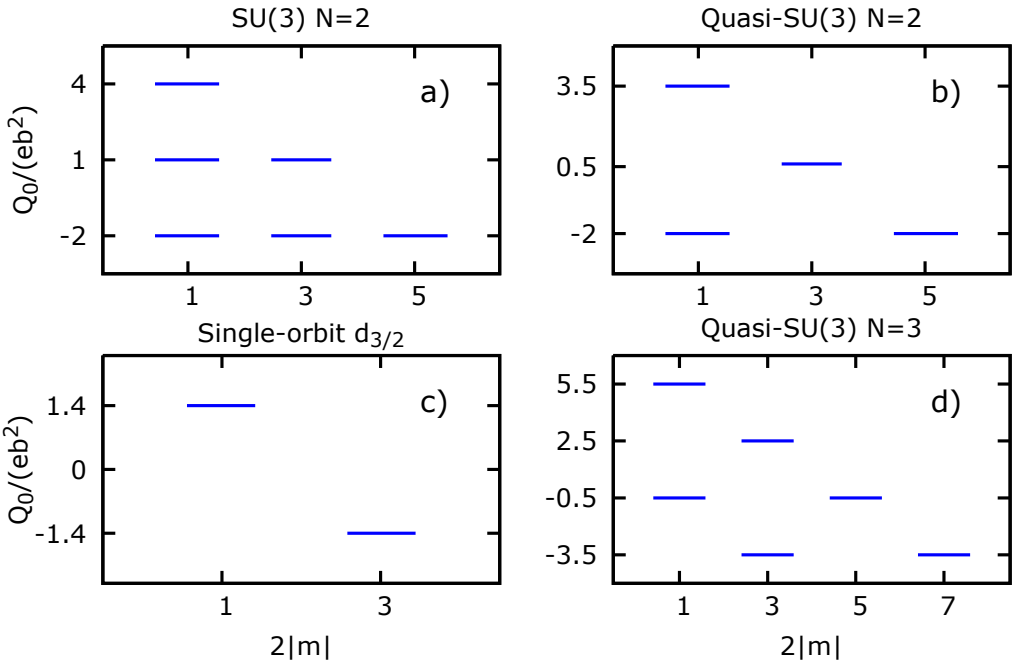

Figure 2.2: Quadrupole diagrams of the different SU(3) variants considered in this work. The dimensionless quadrupole moment $Q_0/(eb^2)$ is represented for each available $2|m|$ value, where m is the projection of the total angular number j. Oblate states are obtained by filling from below and prolate ones from above.

The prolate state of the nucleus is obtained by filling diagram 2.2 a) from the top, where the dimensionless quadruple moment contribution of each nucleon is represented by the y-axis value of each level. Thus, we add up the 4 particles (2 protons and 2 neutrons) in the $Q_0/(eb^2) = 4$ level, and the remaining 8 particles on 2 $Q_0/(eb^2) = 1$ levels. This results in a quadrupole moment of $Q_0/e = (4 \cdot 4 + 4 \cdot 1 + 4 \cdot 1 + 3)b^2 = 27b^2$. It is important to note that a term of $3b^2$ needs to be added in order to match the quadrupole values of ideal rotors [37]. Similarly, the oblate state is constructed by filling the diagram in a bottom-up manner, yielding a quadrupole moment of $Q_0/e = (-2 \cdot 12 - 3)b^2 = -27b^2$. To obtain the physical values, we incorporate the nuclear effective charges $e_Z = 1.5e$ for protons and $e_N = 0.5e$ for neutrons. Multiplying Q_0/e by these charges and the nuclear dimension of $b^2 \simeq 3.42$ fm^2 obtained from Eq. (1.11), we find that

$$|Q_0| = (|Q_{0,Z}| \cdot e_Z + |Q_{0,N}| \cdot e_N + 3e) \cdot b^2 \tag{2.17}$$

$$= (12 \cdot 1.5e + 12 \cdot 0.5e + 3e) \cdot 3.42 \text{ fm}^2 = 92.3\ e \text{ fm}^2. \tag{2.18}$$

Consequently, the SU(3) model predicts ^{28}Si to possess degenerate oblate and prolate states with the aforementioned quadrupole moment values. Nevertheless, the experimental data shows that the ground state is oblate and the prolate state appears almost 7 MeV higher in energy.

The measured deformation for the ground state corresponds to $Q_0 = -57.3 \pm 0.7\ e$ fm^2, which is overestimated by SU(3), and it is clearly oblate. Several factors related to the SU(3) approach are responsible for this discrepancy. First of all, the spin-orbit splitting of the *sd*-shell orbits is neglected, which makes them all degenerate in energy. This scenario is unrealistic since the energy separation between the $1d_{5/2}$-

$2s_{1/2}$ orbits is merely 0.7 MeV, in contrast to the approximately ~ 5 MeV separation observed between the doublet and $1d_{3/2}$ (single-particle energies extracted from the USDB interaction [38, 39]).

To solve this issue, alternative SU(3) schemes sacrifice some degree of symmetry in exchange of a more realistic view [40]. One of the variants of the SU(3) model is the quasi-SU(3) scheme, specifically adapted to accommodate orbitals with $\Delta j = 2$ angular momentum differences. This scheme takes advantage of the fact that $\Delta j = 1$ single-particle matrix elements of $q_0^{(2)}$ are weaker compared to those with $\Delta j = 2$ [41]. An example within the *sd* shell involves the $1d_{5/2}$-$2s_{1/2}$ doublet. Figure 2.2 b) illustrates the Q_0 values corresponding to the quasi-SU(3) model for this doublet.

An additional variation of the SU(3) model is known as the single-orbit limit. This situation occurs when an orbit is significantly separated from the others. For example, the $1d_{3/2}$ orbit is placed between the nearly degenerate $1d_{5/2}$-$2s_{1/2}$ doublet and a major shell closure. The quadrupole moment contribution of a single orbit with total angular momentum j and projection m is [40]

$$Q_0/e = \sum_{m>0} \left(\mathcal{P} + \frac{3}{2}\right) \frac{j(j+1) - 3m^2}{2j(j+1)} b^2, \tag{2.19}$$

which verifies the fact that any filled orbit corresponds to a spherical shape $Q_0 = 0$, as described in the spherical mean field picture. The contribution of a single $1d_{3/2}$ orbit to Q_0 is represented in Fig. 2.2 c).

Given the substantial energy gap between the $1d_{5/2}$-$2s_{1/2}$ doublet and the $1d_{3/2}$ orbit, a $(1d_{5/2}\text{-}2s_{1/2}) + 1d_{3/2}$ prescription holds the greatest physical significance, where the $1d_{5/2}$-$2s_{1/2}$ orbits are treated as degenerate. The particle-hole notation is introduced as np-nh, where n denotes the number of particles that are promoted from the lower space, $1d_{5/2}$-$2s_{1/2}$, to the upper one, $1d_{3/2}$. For instance, filling the levels from Fig 2.2 and recovering the appropriate units, the oblate 0p-0h configuration has intrinsic quadrupole moment

$$Q_0 = (4 \cdot (-2) + 2 \cdot 0.5 - 3) \cdot (0.5 + 1.5)e \cdot 3.42 \text{ fm}^2 = -58.1 \ e \text{ fm}^2, \tag{2.20}$$

and the 4p-4h prolate configuration has

$$Q_0 = (2 \cdot 3.5 + 2 \cdot 0.5 + 2 \cdot 1.4 + 3) \cdot (0.5 + 1.5)e \cdot 3.42 \text{ fm}^2 = 84.1 \ e \text{ fm}^2. \tag{2.21}$$

The quadrupole moments corresponding to remaining prolate and oblate np-nh configurations are indicated in Table 2.1. The significant quadrupole moment observed

Table 2.1: Quadrupole moments (e fm^2) for the experimental GS and ND bands, the possible spherical state and the np-nh configurations in the analytical ($1d_{5/2}$-$2s_{1/2}$)+$1d_{3/2}$ scheme. I also present SU(3) predicted values for prolate and oblate configurations, following Eq (2.17) and Fig. 2.2.

$Q_{0,\text{spherical}}$		$Q_{\text{exp,GS}}$			$Q_{\text{exp,ND}}$	
0		**-57.3±0.7**			**70±7**	
Analytical	0p-0h	2p-2h	4p-4h	6p-6h	8p-8h	Pure SU(3)
$Q_{0,\text{prolate}}$	37.6	60.9	**84.1**	71.1	58.1	**92.3**
$Q_{0,\text{oblate}}$	**-58.1**	-71.1	**-84.1**	-60.9	-37.6	**-92.3**

in the oblate 0p-0h configuration is remarkable due to the substantial correlation gain achieved by the simple addition of the $2s_{1/2}$ orbit, compared to the filled $1d_{5/2}$ spherical picture. The proximity of the $s_{1/2}$ orbit to the $1d_{5/2}$ orbit, coupled with the substantial increase in collectivity, leads the system to prefer an oblate deformed shape over a spherical one.

In the case of the ND prolate band, the primary contenders are the 2p-2h and 4p-4h prolate configurations. The prolate 0p-0h configuration exhibits significantly lower deformation compared to the oblate configuration, rendering it energetically unfavorable. Conversely, prolate np-nh configurations with $n \geq 6$ display lower deformation than the 4p-4h configuration at the expense of promoting more particles. I anticipate that the 4p-4h prolate configuration will prevail over the 2p-2h configuration. This is because both the 2p-2h and 4p-4h configurations yield the same increase in quadrupole moment compared to the prolate 0p-0h configuration. However, since the correlation energy is quadratically related to the quadrupole moment and the single-particle energy of np-nh configurations increases linearly with the number of excited particles, the 4p-4h configuration may be a more favorable candidate, provided that the quadrupole force is strong enough.

2.3 Nuclear shell model

The interacting nuclear shell model, or in short the nuclear shell model (NSM), is a method of solving the nuclear many-body problem formulated as an effective many-body Hamiltonian in a valence space. There are three key features for this method: a relatively small configuration space, an effective interaction and how to solve the Schrödinger equation (2.2).

The necessity of a valence space arises naturally from the approach to the problem itself when dealing with medium-mass or heavy nuclei. Initially, the starting point involves the spherical mean-field, whose states serve as the single-particle basis. However, as the single-particle Hilbert space is infinitely large, the associated many-body space becomes infeasible to handle. Consequently, a boundary is required to render the problem tractable. The simplest solution involves considering a truncation of the Hilbert space, primarily delimited by the major shells of the mean field potential from Eq. (2.4), although only for light nuclei. The large energy gaps between these shells, due to the magic numbers [17], make mixing between them difficult. Nonetheless, selecting the appropriate valence space is more intricate, as certain operators may depend on properties such as parity changes, which cannot be accommodated solely within a major shell.

Moreover, the dimensions of the many-body basis, the Slater determinants, expand combinatorially, rendering some choices of the space numerically unfeasible. This introduces the necessity of an inert core comprising a fraction of the nucleons, which can be represented by a single Slater determinant obtained through the filling of the spherical mean-field levels.

Taking into account all these considerations, the analysis leads us to identify three distinct parts of the single-particle Hilbert space:

1. The **inert core**, which comprises orbits represented by a single Slater determinant that fills up the core particles $A_{\text{core}} = N_{\text{core}} + Z_{\text{core}}$ to a lower boundary of the single-particle Hilbert space.

2. The **valence space**, which encompasses orbits where the remaining nucleons $A_v = N_v + Z_v$ can interact according to the effective interaction.

3. The **empty space**, which consists of orbits that are always assumed to be unoccupied, defined by an upper boundary of the single-particle Hilbert space.

Since we have introduced a change from the original Hamiltonian, defined in the infinite Hilbert space, to a specific valence space, the Hamiltonian must undergo an adaptation to an effective form that suits the problem at hand. Consequently, the effective Hamiltonian $\mathcal{H}_{\text{eff}}$ incorporates the single-particle energies and the two-body matrix elements associated to the orbits within the valence space. This adjustment ensures the appropriate description of the system within the reduced valence space. The effective Hamiltonian captures the effects, such as correlations, that are disregarded in the simplified mean field approach, Eq. 2.3, and can be understood as a residual interaction $\mathcal{H}_{\text{res}}$:

$$\mathcal{H}_{\text{eff}} = \sum_{i}^{A} (t_i + v_i) + \left(\sum_{i,j}^{A} V_{ij} - \sum_{i}^{A} v_i \right) = \mathcal{H}_0 + \mathcal{H}_{\text{res}}. \tag{2.22}$$

In summary, the initial many-body problem is simplified to the task of diagonalizing an effective Hamiltonian within the defined valence space:

$$\mathcal{H}|\Psi\rangle = E|\Psi\rangle \rightarrow \mathcal{H}_{\text{eff}}|\Psi_{\text{eff}}\rangle = E|\Psi_{\text{eff}}\rangle. \tag{2.23}$$

The bare operators also must undergo a transformation to assume a new effective form that suits the characteristics of the valence space

$$\langle\Psi|O|\Psi\rangle \rightarrow \langle\Psi_{\text{eff}}|O_{\text{eff}}|\Psi_{\text{eff}}\rangle. \tag{2.24}$$

The final step involves seeking a suitable method for determining eigenvectors and eigenenergies of the problem.

2.3.1 Exact diagonalization

The first method I have used to solve the many-body Schrodinger equation involves performing an exact diagonalization of the effective Hamiltonian in the valence space [26]. The basis for this method consists of all possible Slater determinants $|\Phi_\alpha\rangle$ that can be built within the valence space, denoted as m-scheme. Then, the eigenstates $|\Psi_{\text{NSM}}\rangle$ are linear combinations of the spherical mean field states

$$|\Psi_{\text{NSM}}\rangle = \sum_{\alpha} C_\alpha |\Phi_\alpha\rangle, \tag{2.25}$$

which is configuration mixing of states. However, it results in a basis with maximal dimensions, which may pose numerical challenges due to the large size of the problem. The number of Slater determinants that can be constructed within a valence space with Ω_i states, where $i = Z$ represents protons and $i = N$ neutrons, and Z_v valence protons and N_v neutrons is

$$\text{dim} = \binom{\Omega_Z}{Z_v} \binom{\Omega_N}{N_v}. \tag{2.26}$$

For instance, a calculation of ^{28}Si in the sd-shell ($\Omega_N = \Omega_Z = 12$) with a core of ^{16}O ($N_v = Z_v = 6$) involves

$$\dim = \binom{\Omega_Z}{Z_v}\binom{\Omega_N}{N_v} = \binom{12}{6}\binom{12}{6} \approx 1 \cdot 10^6, \tag{2.27}$$

which is a dimension that is not demanding for modern computer standards. Nevertheless, a calculation involving the *sd* and *pf* major shells increases the dimension significantly to around

$$\dim = \binom{\Omega_Z}{Z_v}\binom{\Omega_N}{N_v} = \binom{12+20}{6}\binom{12+20}{6} = \binom{32}{6}\binom{32}{6} \approx 1 \cdot 10^{12}, \tag{2.28}$$

which exceeds the scope of this project as even record calculations of $d \approx 1 \cdot 10^{11}$ [42] do not reach the required dimensions. It is important to mention that in practice, these dimensions can be slightly reduced by taking advantage of certain symmetries, for instance not necessitating all the total angular momentum projections, m.

As demonstrated by this example, direct diagonalization of such large matrices is impracticable due to limitations imposed by computer capabilities. Hence, alternative algorithms are implemented such as the Lanczos method. The Lanczos method entails constructing an orthonormal basis by initiating with a pivot state $|\Psi_1\rangle$ and subsequently applying the Hamiltonian operator $\mathcal{H}_{\text{eff}}$ to it. In the first step ($k = 1$):

$$\mathcal{H}_{\text{eff}}|\Psi_1\rangle = E_{11}|\Psi_1\rangle + E_{12}|\Psi_1\rangle, \tag{2.29}$$

where $E_{11} = \langle\Psi_1|\mathcal{H}_{\text{eff}}|\Psi_1\rangle$. Then, E_{12} is obtained by normalization:

$$E_{12}|\Psi_2\rangle = \mathcal{H}_{\text{eff}}|\Psi_1\rangle - E_{11}|\Psi_1\rangle. \tag{2.30}$$

The next step ($k = 2$) involves

$$\mathcal{H}_{\text{eff}}|\Psi_2\rangle = E_{21}|\Psi_1\rangle + E_{22}|\Psi_2\rangle + E_{23}|\Psi_3\rangle. \tag{2.31}$$

Since the Hamiltonian is hermitian $E_{12} = E_{21}$. Then $E_{22} = \langle\Psi_2|\mathcal{H}_{\text{eff}}|\Psi_2\rangle$ and

$$E_{23}|\Psi_3\rangle = (\mathcal{H}_{\text{eff}} - E_{22})|\Psi_2\rangle - E_{21}|\Psi_1\rangle. \tag{2.32}$$

The following steps follow the relation

$$\mathcal{H}_{\text{eff}}|\Psi_k\rangle = E_{kk-1}|\Psi_{k-1}\rangle + E_{kk}|\Psi_k\rangle + E_{kk+1}|\Psi_{k+1},\rangle \tag{2.33}$$

and the normalization is applied in each step. Through this procedure, a tridiagonal matrix is constructed, wherein the mean values of the Hamiltonian appear sequentially. These mean values are regarded as eigenvalues when the difference between each iteration falls below a certain tolerance. It is important to note that the Lanczos iteration process exhibits characteristics similar to those of variational methods, as the eigenvalues converge progressively rather than being immediately exact. However, the convergence of the eigenvalues is highly efficient and exhibits a well-behaved behavior [26]. Therefore, despite not being strictly an exact method, I refer to this approach as an "exact solution" due to its reliable convergence properties. In practice, all states obtained in this work by exact diagonalization are converged in energy to better than 0.5 keV, which exceeds the precision required for nuclear-scale phenomena.

In this work I use the nuclear shell model ANTOINE code [43–45], which performs the exact diagonalization of the effective Hamiltonian by the Lanczos method.

2.3.2 Variational method

The exact diagonalization method provides the most accurate solution to Eq. (2.2) within the valence space. However, its applicability is limited due to the combinatorial scaling of the many-body basis, as shown in Eq. (2.26), which quickly restricts the dimensions of the space. Hence, approximate methods are necessary to solve the eigenvalue problem [46]. The dimensionality issue arises from using all possible Slater determinants in the valence space as the many-body basis. To overcome this challenge, a viable approach is to employ a smaller yet more complex set of wavefunctions obtained through variational techniques. Subsequently, configuration mixing of these variational wavefunctions allows for the determination of approximate solutions instead of exact diagonalization [47].

According to the Ritz variational principle [48], the energy obtained from a trial wavefunction $|\phi_0\rangle$ for the ground state is always higher than or equal to the lowest energy obtained from the exact diagonalization of the Hamiltonian (E_0):

$$E\left[|\phi_0\rangle\right] = \frac{\langle\phi_0|\mathcal{H}_{\text{eff}}|\phi_0\rangle}{\langle\phi_0|\phi_0\rangle} \geq E_0, \tag{2.34}$$

where both energies agree when the trial wavefunction coincides with the exact ground state. Variational methods involve finding the wavefunction that exhibits the closest resemblance to the exact wavefunction within a variational space. This is accomplished by minimizing a set of parameters that determine the characteristics of the possible wavefunctions.

When employing product-like wavefunctions, the implementation of this variational method leads to the formulation of Hartree-Fock equations. However, this assumption is overly restrictive since correlations between particles play a crucial role in describing atomic nuclei. Therefore, in order to expand the variational space, certain symmetries such as particle number, rotational invariance or parity are intentionally broken. For instance, to incorporate pairing correlations between fermions, the independent particle description is modified to include quasiparticles, which results in a violation of the conservation of particle number. This approach is the Hartree-Fock-Boguliubov (HFB) method [49], where the HFB wavefunction $|\phi_{\text{HFB}}\rangle$ is the vacuum of a set of fermionic operators β_k:

$$\beta_k|\phi_{\text{HFB}}\rangle = 0 \rightarrow |\phi_{\text{HFB}}\rangle = \prod_k \beta_k|-\rangle;\ \forall k = 1, .., \mathcal{M}, \tag{2.35}$$

where $\mathcal{M}$ is the number of single-particle states of the valence space, and $|-\rangle$ is the true vacuum. The HFB transformation is defined as

$$\beta_k^\dagger = \sum_l (U_{lk}c_l^\dagger + V_{lk}c_l), \tag{2.36}$$

$$\beta_k = \sum_l (U_{lk}^* c_l + V_{lk}^* c_l^\dagger) \tag{2.37}$$

with U_{lk} and V_{lk} matrices that define the state and act as the variational parameters and $c_l^\dagger$ (c_l) the creation (annihilation) operators of a single particle basis. In this work, I am using the TAURUS code [21], which employs the spherical mean field levels as the single particle basis and considers real U and V matrices.

As the transformation itself violates the conservation of particle number, it becomes essential to implement constraints to conserve quantities at the mean-field level. This is achieved by modifying the energy functional to minimize

$$\mathcal{H}'_{\text{eff}} = \mathcal{H}_{\text{eff}} - \lambda_Z O_Z - \lambda_N O_N - \sum_i \lambda_i O_i, \tag{2.38}$$

where O_Z and O_N are particle number operators for the protons and neutrons spaces, respectively, and λ_i are the Lagrange multipliers. Additional constraints such as quadrupole moments or parity correlations can be added to respect the expectation value of any given operator O

$$\langle O \rangle \equiv \langle \phi_{\text{HFB}} | O | \phi_{\text{HFB}} \rangle. \tag{2.39}$$

The minimization process is carried out using a gradient method, with the following schematic procedure. It begins with an initial trial wavefunction $|\phi_0\rangle$ defined by the HFB matrices (U_0, V_0). These matrices can be defined to preserve any desired symmetry, such as spherical symmetry, axial symmetry, or parity. Afterwards, the gradient of the energy is computed, and a direction for minimization is determined. A new wavefunction is proposed, and if it minimizes the Hamiltonian, it is retained. This iterative process continues until convergence is achieved. For a more detailed understanding, refer to [21].

In this study, the focus is on investigating the shapes displayed by ^{28}Si. To explore the energy surfaces associated with possible deformations, constraints on the quadrupole moments are utilized, as defined in section 1.2. Rather than imposing constraints directly on the quadrupole moments $\langle \overline{Q}_{20} \rangle$ and $\langle \overline{Q}_{22} \rangle$, the restrictions are applied to the deformation parameters (β, γ). Additionally, the constraint $\langle \overline{Q}_{21} \rangle = 0$ is included, so the definitions made in Section 1.2 hold.

To restore the symmetries violated by the previously obtained HFB functions $|\phi_{\text{HFB}}\rangle$, quantum number projection is required. This involves restoring proton number, neutron number, and total angular momentum. The HFB wavefunctions can be expressed as linear combinations of states with good quantum numbers:

$$|\phi_{\text{HFB}}\rangle = \sum_{N,Z,J} a_{N,Z,J} |\phi^{N,Z,J}\rangle. \tag{2.40}$$

To obtain symmetry-conserving wavefunctions, the corresponding projectors (P^O) are applied to the HFB states

$$|\phi^{N,Z,J}\rangle = P^N P^Z P^J_{MK} |\phi_{\text{HFB}}\rangle. \tag{2.41}$$

The particle number projectors for neutrons and protons are

$$P^N = \frac{1}{2\pi} \int_0^{2\pi} e^{i\varphi_N (N-N)} d\varphi_N \ , \tag{2.42}$$

$$P^Z = \frac{1}{2\pi} \int_0^{2\pi} e^{i\varphi_Z (Z-Z)} d\varphi_Z, \tag{2.43}$$

with φ_N and φ_Z being the gauge angle, associated to this U(1) symmetry. Finally, the restoration of good total angular momentum involves

$$P^J_{MK} = \frac{2J+1}{16\pi^2} \int_\Omega D^{J*}_{MK} R(\Omega) d\Omega, \tag{2.44}$$

where D^{J*}_{MK} are the Wigner D matrices [25] with M and K the third components of J in the laboratory and intrinsic frames of reference, as explained in section 1.1. Then, the SO(3) rotation operator is $R(\Omega) = e^{-i\alpha J_z} e^{-i\beta J_y} e^{-i\gamma J_z}$, with $\Omega \equiv (\alpha, \beta, \gamma)$ the Euler angles [49].

The expected value of an operator O of the projected states can be calculated as

$$\langle O^{NZJ} \rangle = \frac{\langle \phi | O P^N P^Z P^J_{MK} | \phi \rangle}{\langle \phi | P^N P^Z P^J_{MK} | \phi \rangle}, \tag{2.45}$$

where I have used that $(P^i)^2 = P^i$, $(P^i)^\dagger = P^i$ and the fact that the involved operators commute with each other. The restoration of symmetries in the HFB wavefunctions is computationally the most demanding step in this variational process, as it requires the evaluation of multiple numerically intensive integrals.

Having obtained a set of wavefunctions with well-defined quantum numbers and different deformations, they can be employed to approximate an exact solution by considering linear combinations of states characterized by different deformation parameters, akin to configuration mixing in exact diagonalization. This approach is known as the generator-coordinate method (GCM), where the generator coordinates (q) are represented by the deformation parameters (β, γ). The GCM wavefunction can be expressed as

$$|\Psi^{NZJM}_{\sigma,\mathrm{GCM}}\rangle = \sum_{qK} f^{JMNZ}_{\sigma;qK} P^N P^Z P^J_{MK} |\phi_{\mathrm{HFB}}(q)\rangle, \tag{2.46}$$

where $|\phi_{\mathrm{HFB}}(q)\rangle$ are the unprojected HFB wavefunctions, $f^{JMNZ}_{\sigma;qK}$ is the coefficient of each projected wavefunction and σ orders the states with the same quantum numbers $\Gamma \equiv NZJM$. However, the set of states considered might be linearly dependent, which requires a previous diagonalization of the norm overlap matrix

$$\mathcal{N}^\Gamma_{qKq'K'} = \langle \phi_{\mathrm{HFB}}(q, K) | P^N P^Z P^J_{KK'} | \phi_{\mathrm{HFB}}(q', K') \rangle \tag{2.47}$$

to find an independent basis, denoted as the natural basis:

$$\sum_{q'K'} \mathcal{N}^\Gamma_{qKq'K'} u^\Gamma_{\lambda;q'K'} = n^\Gamma_\lambda u^\Gamma_{\lambda;qK}. \tag{2.48}$$

In principle, the diagonalization of the overlap matrix would yield a spectrum of non-zero eigenvalues, corresponding to linearly independent natural basis states, as well as null eigenvalues that represent linear combinations of the independent basis states. However, due to the use of numerical methods in the diagonalization process, it becomes challenging to distinguish between small eigenvalues and true zero eigenvalues due to numerical errors. In practice, only eigenstates $u^\Gamma_{\lambda;qK}$ with eigenvalues n^Γ_λ above a certain threshold, typically in the range of $n^\Gamma_\lambda \approx 10^{-10}$, are taken into account. However, the specific threshold value is arbitrary, and including more states than necessary can result in numerical difficulties that lead to divergence of operator mean values [50].

Figure 2.3 displays the convergence behavior of the first three 0^+ states of ^{20}Ne. It is evident that as more states are included in the natural basis, the difference between the exact diagonalization and the variational approach decreases. Specifically, when

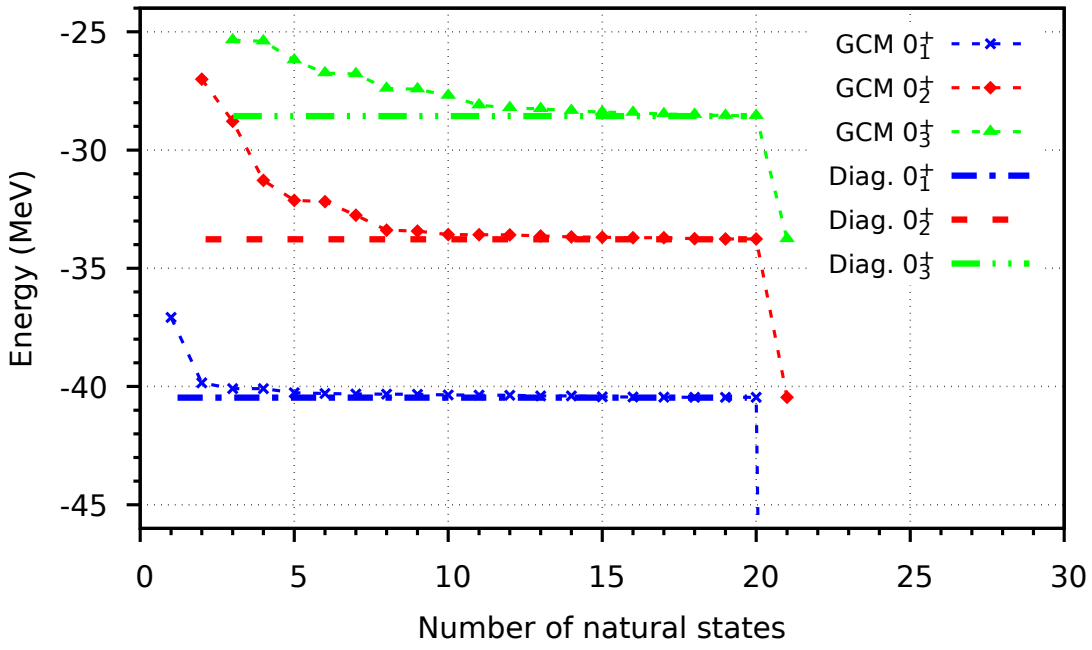

Figure 2.3: Energy evolution of the first three 0^+ states in ^{20}Ne with the GCM method as the number of included natural states increases using the USDB interaction. The exact energies are shown in thick dashed lines.

20 states of the natural basis are considered, out of the initial 47 projected HFB wavefunctions, the discrepancy reaches nearly 10 keV. However, upon including additional states, there is a sharp decline in the energy of the ground state (85 MeV), which falls below the value obtained from exact diagonalization. This sudden drop in energy is also observed for the other excited states. Such behavior serves as an indication that the employed basis exhibits issues such as linear dependence.

With the choice of a threshold, the natural basis states are

$$|\Lambda_\lambda^\Gamma\rangle = \sum_{q'K'} \frac{u^\Gamma_{\lambda;q'K'}}{(n^\Gamma_\lambda)^{1/2}} P^N P^Z P^J_{MK} |\phi_{\mathrm{HFB}}(q)\rangle. \tag{2.49}$$

Then, the GCM wavefunction in the natural space is

$$|\Psi^\Gamma_{\sigma,\mathrm{GCM}}\rangle = \sum_\lambda G^\Gamma_{\sigma;\lambda} |\Lambda^\Gamma_\sigma\rangle \tag{2.50}$$

and the coeficients $G^\Gamma_{\sigma;\lambda}$ are determined solving the Hill-Wheeler-Griffin (HWG) equation

$$\sum_{\lambda'} \langle \Lambda^\Gamma_\lambda | \mathcal{H}_{\mathrm{eff}} | \Lambda^\Gamma_{\lambda'} \rangle G^\Gamma_{\sigma;\lambda'} = E^\Gamma_\sigma G^\Gamma_{\sigma;\lambda}, \tag{2.51}$$

which is also an eigenvalue problem. In addition to the energies of the GCM states, the mean value of any given operator can be obtained as

$$\langle \Psi^\Gamma_\sigma | O | \Psi^{\Gamma'}_{\sigma'} \rangle = \sum_{\lambda\lambda'} \sum_{qKq'K'} G^{\Gamma *}_{\sigma;\lambda} \frac{u^{\Gamma *}_{\lambda;qK}}{(n^\Gamma_\lambda)^{1/2}} \langle \phi^\Gamma(q) | O | \phi^{\Gamma'}(q') \rangle G^{\Gamma'}_{\sigma';\lambda'} \frac{u^{\Gamma'}_{\lambda';q'K'}}{(n^{\Gamma'}_{\lambda'})^{1/2}}. \tag{2.52}$$

Among these operators, the electromagnetic transitions and quadrupole moments can be evaluated to explore the deformations of different GCM states for a given nucleus.

Finally, the probability of finding the GCM state in one of its HFB states can be calculated using the collective wave functions

$$|F^{\Gamma}_{\sigma}(q)|^2 = |\sum_{K\lambda} G^{\Gamma}_{\sigma;\lambda} u^{\Gamma}_{\lambda;qK}|^2. \tag{2.53}$$

Taurus [47] is a numerical suite that incorporates the complete variational process outlined in this section. Initially, the quadrupole-constrained HFB wavefunctions are generated. Then, the projection onto good quantum numbers is carried out. Finally, the GCM is used to combine the projected HFB functions and generate the complete ^{28}Si states.

3. Shape coexistence in ^{28}Si

In this section I describe the properties of ^{28}Si employing the nuclear theory techniques discussed in Section 2. The section is organized based on the different collective structures either observed or proposed in previous works among the low-lying states of ^{28}Si. These structures include the observed oblate rotational band associated with the ground state (Section 3.1), the measured prolate rotational band (Section 3.2), and the potential existence of a superdeformed structure (Section 3.3).

3.1 Ground state and oblate band

The ground state of ^{28}Si cannot be adequately explained by a simplistic spherical mean-field model, wherein the nucleons occupy the $1d_{5/2}$ orbit and the nucleus adopts a purely spherical shape. By incorporating particles into the $2s_{1/2}$ orbit using the analytical SU(3) model, which takes into account the nearly degenerate $1d_{5/2}$-$2s_{1/2}$ doublet, significant quadrupole correlations are gained ($Q_0 = -58.1\ e\ \mathrm{fm}^2$). These correlations establish the oblate deformation ($\beta \simeq -0.21$) as the ground state in ^{28}Si, which is in agreement with the experimental data [15] as indicated in Table 2.1.

However, to gain further insight in the structure of ^{28}Si I employ state-of-the-art shell model calculations with an exact diagonalization performed using the ANTOINE code [43], and a variational method using the TAURUS suite [21, 47]. Both methods are implemented within a valence space that encompasses the *sd* shell (Figure 2.2) and utilize the USDB interaction [38], which is the established effective interaction for this space. For electromagnetic properties, I assume the standard effective nuclear charges for the *sd* shell: $e_Z = 1.5e$ and $e_N = 0.5e$. The inert core consists of a ^{16}O nucleus, while the remaining 12 particles interact with each other explicitly within the valence space.

First, I discuss the variational approach to solving the many-body problem. As I have shown in section 2.3.2, the initial step is to generate a a set of quadrupole-constrained HFB wavefunctions. The constraints are imposed on the particle numbers $\langle N_v \rangle = \langle Z_v \rangle = 6$ and the quadrupole parameters ($0 \leq \beta \leq 0.27,\ 0^\circ \leq \gamma \leq 60^\circ$) with spacing of $\delta_\beta = 0.02$ and $\delta_\gamma = 15^\circ$ respectively. In addition, I constrain $\langle \overline{Q}_{21} \rangle = 0$, to be consistent with the definitions of Section 1.2.

Figure 3.1 (left panel) presents the unprojected energy surface. The plot shows that the absolute minimum energy corresponds to an oblate shape ($\gamma = 60^\circ$). Meanwhile, prolate shapes ($\gamma = 0^\circ$) are energetically disfavoured, even when compared to spherical shapes ($\beta \simeq 0$). Based on these results, the ground state acquires an oblate deformation with $\beta \simeq -0.24$, which aligns with the predictions of the SU(3) model as well as experimental observations.

However, these HFB wavefunctions mix states with good quantum numbers, thus requiring projection to obtain well-defined quantum number states. In our basis,

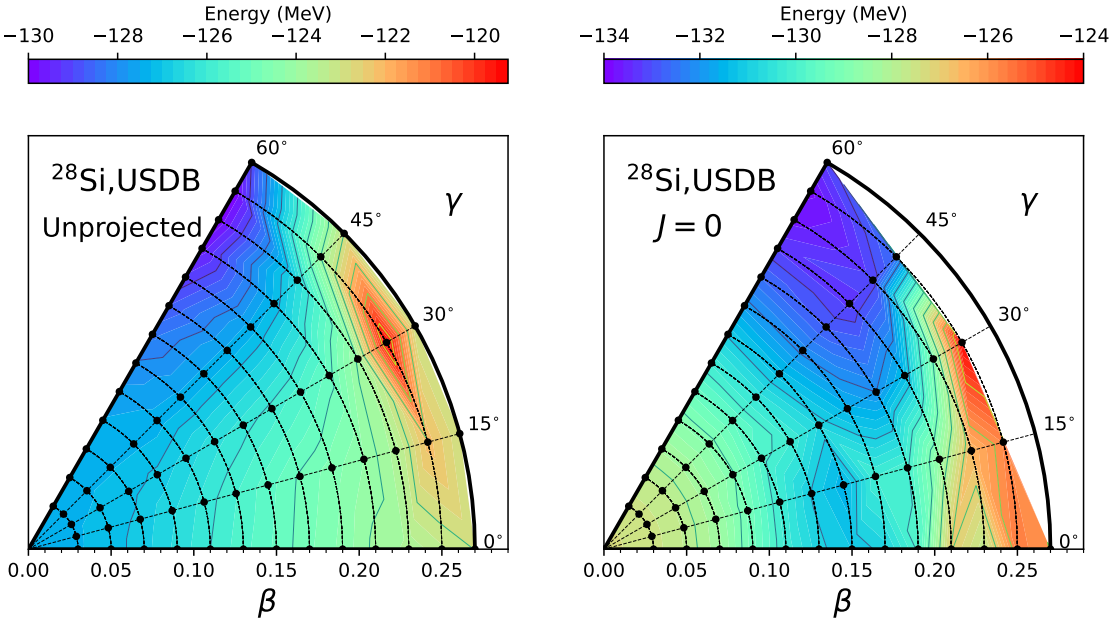

Figure 3.1: Energy surfaces of ^{28}Si in the (β, γ) plane using the USDB interaction for the unprojected (left) and projected to $J = 0$ (right) quadrupole-constrained HFB wavefunctions. Each black circle represents a HFB wavefunction of the mesh.

there are 66 HFB states, and the integrals involving the gauge angles of the particle numbers, Eq. (2.43), are discretized into 10 points, while those involving Euler angles, Eq. (2.44), are discretized into 16 points. Parity projection is not considered as all orbits of the *sd* shell have positive parity. This projection process requires a day of computation, in contrast to the minutes it takes to obtain the unprojected HFB basis, making it the computationally most demanding step. During the projection process, certain states may encounter numerical challenges associated with the evaluation of involved integrals. In my calculations, I have excluded the HFB wavefunctions with $\beta = 0.27$ and $\gamma = 15°$, $30°$, and $45°$ because they did not contain any contribution with $J = 0$.

Figure 3.1 (right panel) shows the results of the energy surface projected to $J = 0$. First and foremost, it is important to highlight that the restoration of symmetries leads to a reduction in the energy of the states [51], by removing artificial constraints and restoring physical symmetries in the model. The absolute minimum remains oblate with a similar deformation of approximately $\beta \simeq -0.25$, similar to the unprojected case. However, in the projected results, two additional minima appear in the prolate region at $\beta \simeq 0.15$, with a skew towards $\gamma = 15°$, and at $\beta \simeq 0.22$. When applying projection to $J = 0$, the spherical state is found to be energetically more unfavorable.

The final step involves the GCM to perform configuration mixing of the quadrupole-constrained HFB states. As discussed in Section 2.3.2, it is necessary to find an orthogonal basis due to the potential presence of linear dependencies among the considered projected HFB wavefunctions. For this purpose the overlap matrix is diagonalized following Eq. (2.48). Subsequently, using the orthogonal states referred to as the natural basis, the HWG equation (2.51) is solved to determine the eigenvalues and eigenstates. The criterion to determine the threshold for the linear

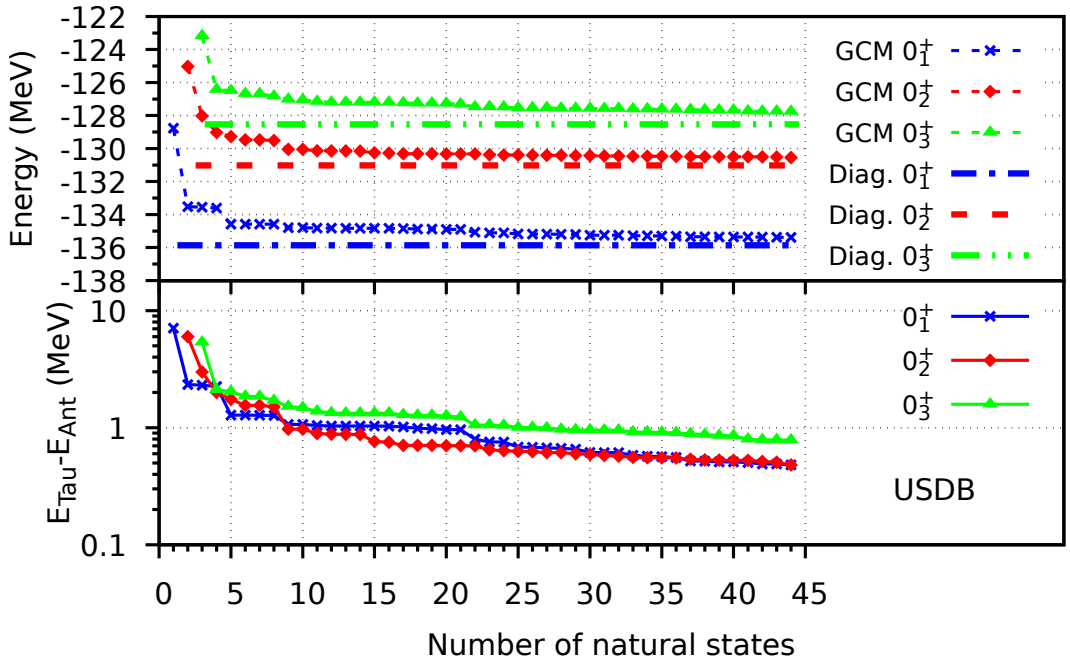

Figure 3.2: (Top panel) Energy evolution of the first three 0^+ states in ^{28}Si with the GCM method as the number of included natural states increases using the USDB interaction. The calculated values using exact diagonalization (Diag.) are indicated with horizontal lines. (Bottom panel) Energy difference between the GCM and exact diagonalization as a function of the number of natural states.

independence of the states of the natural basis is determined with the convergence of the energies. Figure 3.2 (Top) shows the energy of the first three 0^+ states of ^{28}Si with respect to the number of natural states included. My findings indicate that out of the 63 HFB wavefunctions considered, only 44 form a stable and well-behaved basis. However, when an additional state is included in the natural basis, the presence of linear dependencies leads to an energy divergence. The energy convergence follows a plateau-like pattern, where each state has lower energy than the previous one since it is a variational approach.

It is important to note that the variational approach is an approximate solution to the diagonalization of the effective interaction, Eq. (2.23). Therefore, to validate the results, I have conducted the exact diagonalization of the Hamiltonian using the ANTOINE code, as described in Section 2.3.1. The energy values for the first three 0^+ states obtained from exact diagonalization are also presented in Fig. 3.2. The difference between the two methods is approximately 1 MeV, which is a reasonable outcome for a complex nucleus like ^{28}Si. In comparison, I have used ^{20}Ne as a benchmark for the variational method, where the energy difference between the two methods is only a few keV. To calculate $J \neq 0$ states in the variational approach, I follow the same procedure with the only difference being that the basis is formed with $(2J+1) \cdot 63$ states, resulting from the projections of the total angular momentum.

As discussed in Section 2.3.2, it is possible to calculate collective wavefunctions, which indicate the contribution of a given HFB basis state to the mixed wavefunction, in order to visualize the shape of a GCM state. Fig. 3.3 displays the collective wavefunctions of the first $J = 0$, $J = 2$, and $J = 4$ states, illustrating the contribu-

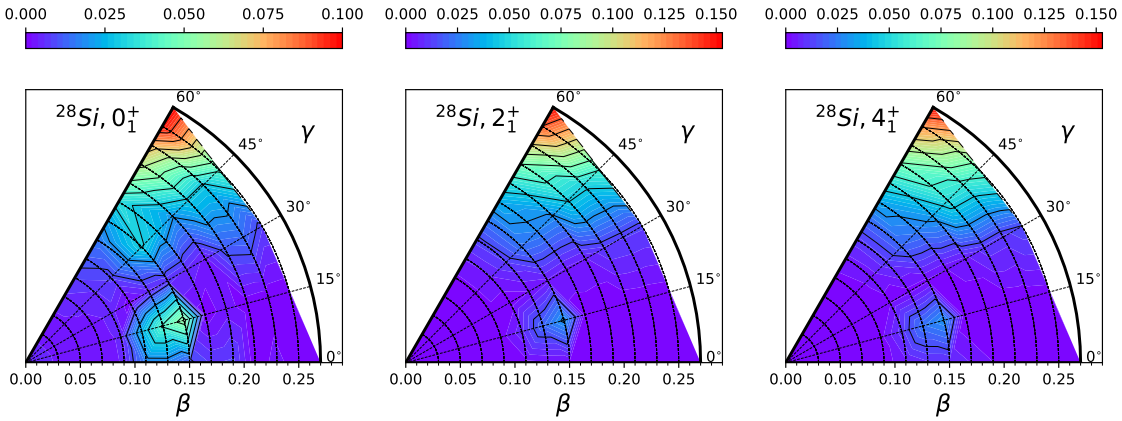

Figure 3.3: Collective wavefunctions of the lowest-energy three states of the oblate rotational band in ^{28}Si, calculated using the USDB interaction.

tion of specific projected HFB wavefunction to the configuration-mixed state. The ground state ($J^\pi_\sigma = 0^+_1$) primarily occupies the region of highest oblate deformation, with $\beta = -0.27$. However, it also exhibits some contribution from the $\beta = 0.15$ minimum. A comparison of the collective wavefunctions shows that the 0^+_1 state serves as the bandhead of an oblate rotational band becomes apparent when examining the collective wavefunctions of the 2^+_1 and 4^+_1 states. This is because they share the same intrinsic deformation, as discussed in Section 1.1.

In order to provide additional evidence for the existence of this rotational band, I calculate the $B(E2)$ transition strengths between the states within the oblate band. The results for the B(E2) transition strengths, obtained using both methods, the exact diagonaliztation and the variational method, and compared to the experimental values, are presented in Fig 3.4 (blue bands). First and foremost, there is an excellent agreement between the variational approach and the exact diagonalization method, giving even more confidence in the previous energy. Secondly, the $B(E2)$ values are large and correspond to $\beta \approx \pm 0.23$ following Eq. 1.16, where the USDB interaction slightly overestimates the experimental deformation $\beta \approx -0.20$. Finally, the ratio $B(E2, 4^+_1 \to 2^+_1)/B(E2, 2^+_1 \to 0^+_1) = 1.41$ is in agreement with the theoretical one

$$\frac{B(E2, 4^+_1 \to 2^+_1)}{B(E2, 2^+_1 \to 0^+_1)} = \frac{\langle 4200|20\rangle^2}{\langle 2200|00\rangle^2} = 1.43,$$

where I have considered that Q_0 is constant in Eq. (1.16), since states of a rotational band share the same deformation. However, there is a discrepancy in the level spacing, as the calculated value of $E_{\rm ex}(4^+_1)/E_{\rm ex}(2^+_1) = 4.6/1.9 = 2.42$, which is similar to the experimental value, differs from the theoretical prediction for a perfect rotor of

$$\frac{E_{\rm ex}(4^+_1)}{E_{\rm ex}(2^+_1)} = \frac{4 \cdot (4+1)}{2 \cdot (2+1)} = \frac{10}{3} \simeq 3.33,$$

where $E_{\rm ex}(J^\pi_\sigma) = E(J^\pi_\sigma) - E(J^\pi_0)$ is the excitation energy of the state.

In regards to the vibrational band, the collective wavefunction of the 0^+_2 state is also oblate and centered in $\beta = -0.27$. Thus, it is consistent with a β-vibration of the ground state, as proposed in [16].

To complement these results, I have computed the quadrupole moments of fixed np-nh configurations with the USDB interaction with the exact diagonalization,

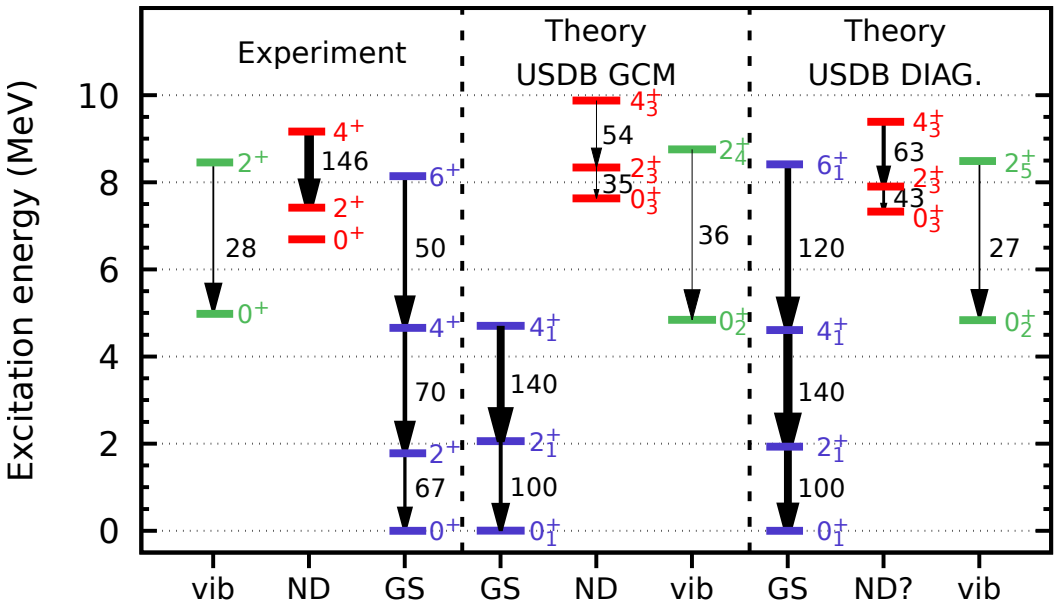

Figure 3.4: Band structure of the lowest-lying positive parity states of ^{28}Si: left, experiment [15]; center, calculation using the USDB interaction with the TAURUS suite and right, calculation using ANTOINE. The arrows indicate in-band $B(E2)$ transition strengths (e^2 fm^4), with larger values associated to more deformed shapes. The labels "vib", "ND" and "GS" stand for vibrational band, normal deformed band and ground state, respectively.

indicated in Table 3.1. The 0p-0h configuration is oblate and the remaining ones are prolate, however the 2p-2h and 8p-8h configurations are not well established as the intrinsic quadrupole moments extracted from the spectroscopic quadrupole moments (Eq. 1.14) or from the $B(E2, 2^+ \to 0^+)$ (Eq. 1.16) transition strengths differ. The 0_1^+ state has a larger deformation $Q_{0,t} = \pm 70.7$ and $Q_{0,s} = -73.0$ than the oblate 0p-0h configuration with $Q_{0,t} = \pm 41.6$ and $Q_{0,s} = -45.7$. This is corroborated by examining the average occupation numbers of each orbit. For the 0_1^+ state, the USDB average occupation numbers are approximately 9.32 particles in the $1d_{5/2}$ orbit, 1.25 particles in the $s_{1/2}$ orbit (30% filled), and 1.43 particles in the $1d_{3/2}$ orbit (15% filled). In contrast, for a spherical state, we would expect all 12 particles to be in the $1d_{5/2}$ orbit, and for the 0p-0h configuration of the quasi-SU(3) scheme, the $1d_{3/2}$ orbit should be unoccupied. It is evident that the situation is quite involved, and the analytical approaches serve as mere approximations to capture the complexity of the system.

Table 3.1: Quadrupole moments (e fm^2) the np-nh configurations in the shell model numerical calculations. We also present the numerical GS and the possible ND band results obtained with the USDB interaction.

Numerical	0p-0h	2p-2h	4p-4h	6p-6h	8p-8h	GS	ND?
$Q_{0t,\mathrm{USDB}}$	$\pm$**41.6**	$\pm$49.4	$\pm$**68.2**	$\pm$53.9	$\pm$45.2	$\pm$**70.7**	$\pm$**46.6**
$Q_{0s,\mathrm{USDB}}$	**-45.7**	16.0	**66.4**	46.4	9.8	**-73.0**	**31.2**

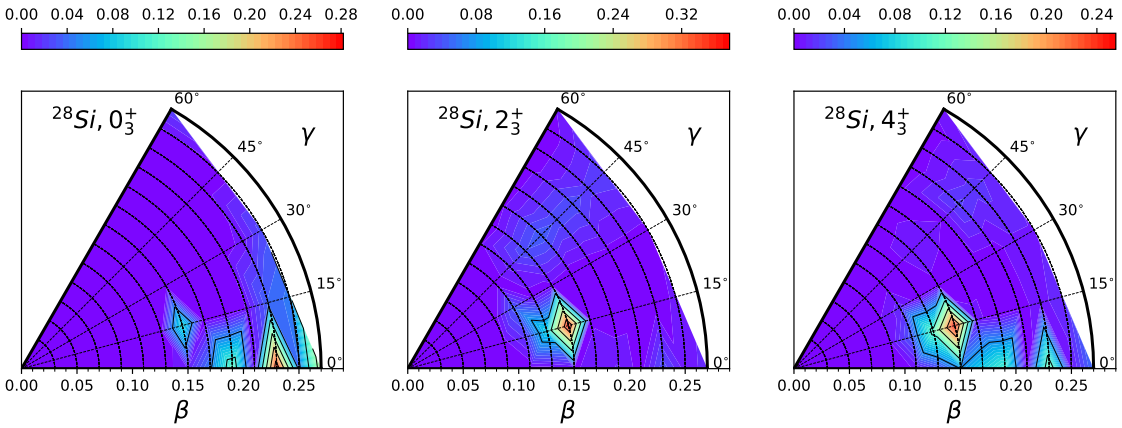

Figure 3.5: Collective wavefunctions of the first three states of the prolate rotational band in ^{28}Si, calculated using the USDB interaction.

3.2 Prolate band and modification of the interaction

Moving to the prolate region, the experimental data suggests the presence of a normal deformed (ND) prolate band, as highlighted in Fig. 3.4. The level spacing follows a proportionality to $J(J+1)$ and the measured $B(E2)$ transition strength from the corresponding $4^+ \rightarrow 2^+$ states indicates a deformation of $\beta \approx 0.23$. From the exact diagonalization and GCM calculations with the USDB interaction, I do not find any $B(E2)$ that matches the experimental result. The ones that most closely resemble this structure are indicated in red in Fig. 3.4, with $B(E2, 4_3^+ \rightarrow 2_3^+)$ values corresponding to a shape with $\beta \approx 0.15$. Although the states follow a band structure, these states display weak $B(E2)$ values and are slightly higher in energy.

The exact diagonalization and variational approaches suggest the same results, despite the variational method indicating a marginally lower deformation indicated by weaker $B(E2)$ transitions and higher energy. To gain insight on the shapes that correspond to these states, I represent the collective wavefunctions in Fig. 3.5. The $J_\sigma^\pi = 0_3^+$ state has most of its contribution coming from the $\beta = 0.23$ region. However, the 2_3^+ and 4_3^+ states are mainly in the $\beta = 0.15$ minimum. This observation is consistent with the low values of $B(E2)$ transitions, as the 2_3^+ and 4_3^+ states exhibit low deformation, and the 0_3^+ and 2_3^+ states are situated in distinct regions. It is worth noting that these three states are the ones that most closely resemble a prolate-shaped rotational band. The other states present in the spectrum are excluded either due to lower $B(E2)$ values or their failure to follow the $J(J+1)$ proportionality. From this discussion, I conclude that the USDB interaction fails at establishing a well-behaved prolate band.

Based on the analytical SU(3)-based models, we have seen that the 4p-4h prolate configuration is the most favorable candidate for establishing a ND band. This conclusion is further supported by the numerical np-nh configurations presented in Table 3.1 studied with exact diagonalization. In contrast, the 2p-2h configuration fails to satisfy $Q_{0,s} \approx Q_{0,t}$. In order to find what happens to this 4p-4h prolate configuration $|0^+_{4p-4h}\rangle_{sd}$, we can utilize it as a pivot state to initialize the exact diagonalization of the interaction in the full sd space, observing how it distributes

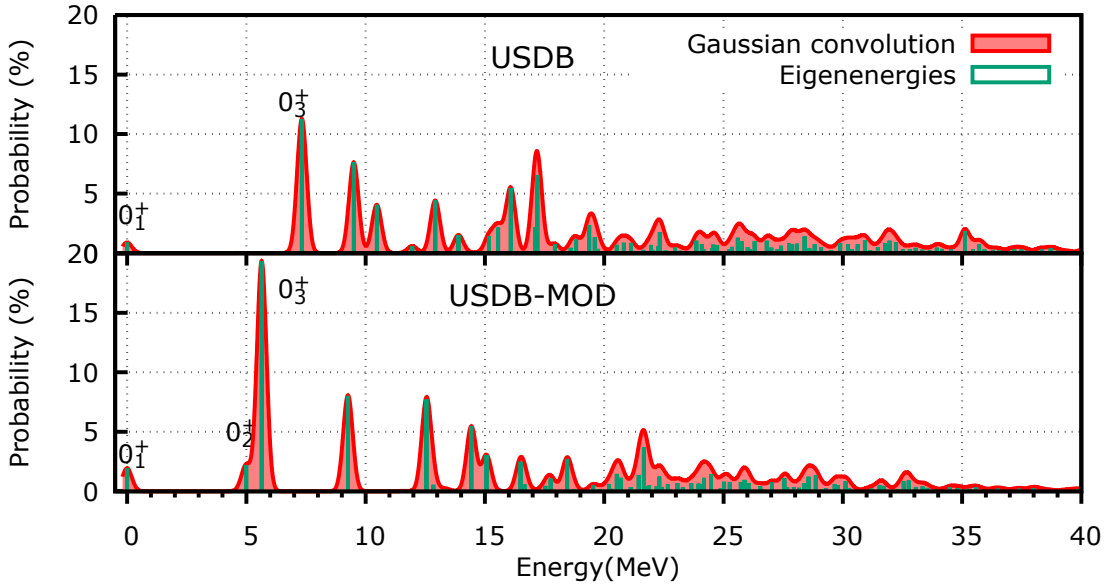

Figure 3.6: Probability (%) of finding the lowest energy state with fixed 4p-4h configuration $|0^+_{\text{4p-4h}}\rangle_{sd}$ in the full *sd*-shell states $|0^+_\sigma\rangle_{sd}$ with the USDB interaction (top panel) and the USDB-MOD interaction (bottom panel). Each eigenstate is convoluted with Gaussians of 200 keV width.

among the resulting mixed states $|0^+_\sigma\rangle_{sd}$:

$$|0^+_{\text{4p-4h}}\rangle_{sd} = \frac{1}{N}\sum_\sigma S(\sigma)|0^+_\sigma\rangle_{sd}, \tag{3.1}$$

where N is the normalization factor and $S^2(\sigma)$ is the so-called Lanczos strength function, which denotes the probability of finding the lowest energy state with fixed 4p-4h configuration in the full *sd*-shell states. This approach reveals the fragmentation of the 4p-4h prolate configuration among the diagonalized states, as illustrated in the top panel of Figure 3.6. The results obtained with the USDB interaction are shown in the top panel, where the 0^+_3 state contains about a 10% component from the 4p-4h configuration. The presence of this component alone is insufficient to generate a coherent rotational band that can be directly associated with the experimental observations.

Based on the previous discussion, the 4p-4h prolate configuration does not produce the expected well-behaved normal deformed band with the USDB interaction, contrary to what is observed in experimental data. One possible explanation for this discrepancy is that the increase in correlation energy is insufficient to compensate for the promotion of four particles from the $d_{5/2}$-$s_{1/2}$ doublet to the $d_{3/2}$ orbit. To favor the formation of this 4p-4h configuration suggested by the analytical model, which aligns with the experimental data in terms of deformation, I propose lowering the energy gap between the $d_{5/2}$-$s_{1/2}$ and $d_{3/2}$ orbits. Specifically, I modify the single-particle energy of the $d_{3/2}$ orbit, denoted as $\epsilon(d_{3/2})$, from 2.2 MeV to 0.9 MeV, while keeping $\epsilon(d_{5/2}) = -3.9$ MeV and $\epsilon(s_{1/2}) = -3.2$ MeV unchanged. The modified interaction leads to a new effective interaction denoted from now on as USDB-MOD.

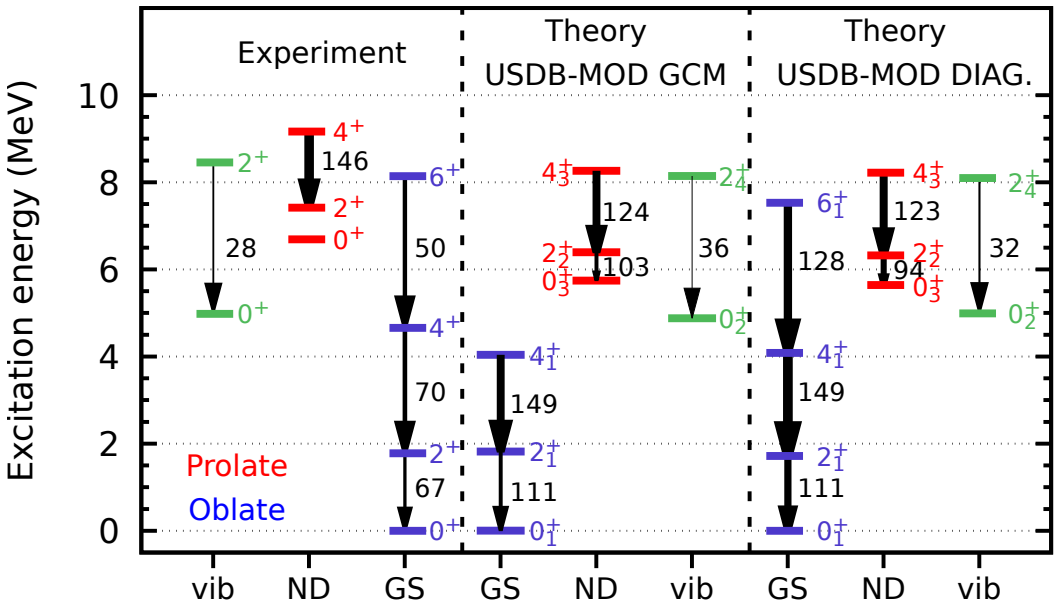

Figure 3.7: Band structure of the lowest-lying positive parity states of ^{28}Si: left, experiment [15]; center, calculation using the USDB-MOD interaction with the TAURUS suite and right, using USDB-MOD.

It has no impact on the quadrupole moment of the np-nh configurations presented in Table 3.1. Instead, it enables the structure to withstand configuration mixing within the complete *sd* space. It is worth noting that this change is relatively small, affecting only $\epsilon(d_{3/2})$ among the three single-particle energies and the 63 two-body matrix elements that constitute the USDB interaction [38].

By employing the USDB-MOD interaction and conducting an exact diagonalization, I have obtained the states shown in Figure 3.7 (right). Notably, the transition $B(E2, 4_3^+ \rightarrow 2_2^+)$ now corresponds to 123 e^2 fm^4, in very good agreement with the experimental value. Furthermore, the states 0_3^+, 2_2^+, and 4_3^+ exhibit a clear proportionality to $J(J+1)$. Due to the modification that reduces the energy cost of promoting particles to the $d_{3/2}$ orbit, the prolate band head lies at a lower energy level compared to the USDB interaction. While the oblate band and its vibration experience some additional collectivity, their overall properties remain largely similar to the results obtained with the USDB interaction. Consequently, by lowering the $d_{3/2}$ orbit, I have successfully established a well-defined prolate band while introducing only minor alterations to the oblate band and its vibration.

In order to gain a better understanding of the structure of the newly found prolate band, I conduct a variational calculation using the USDB-MOD interaction. The resulting energy surfaces, both unprojected and projected to $J = 0$, are presented in Figure 3.8. In comparison to the USDB results, the unprojected surface exhibits a more pronounced oblate minimum, while the prolate region appears to be relatively flatter. When considering the projected surface, the preference for a spherical shape diminishes further, and the prolate minimum at $\beta = 0.23$ is no longer discernible.

Using the projected HFB states as a basis, I use the GCM to determine the configuration-mixed eigenstates of ^{28}Si with the USDB-MOD interaction. The con-

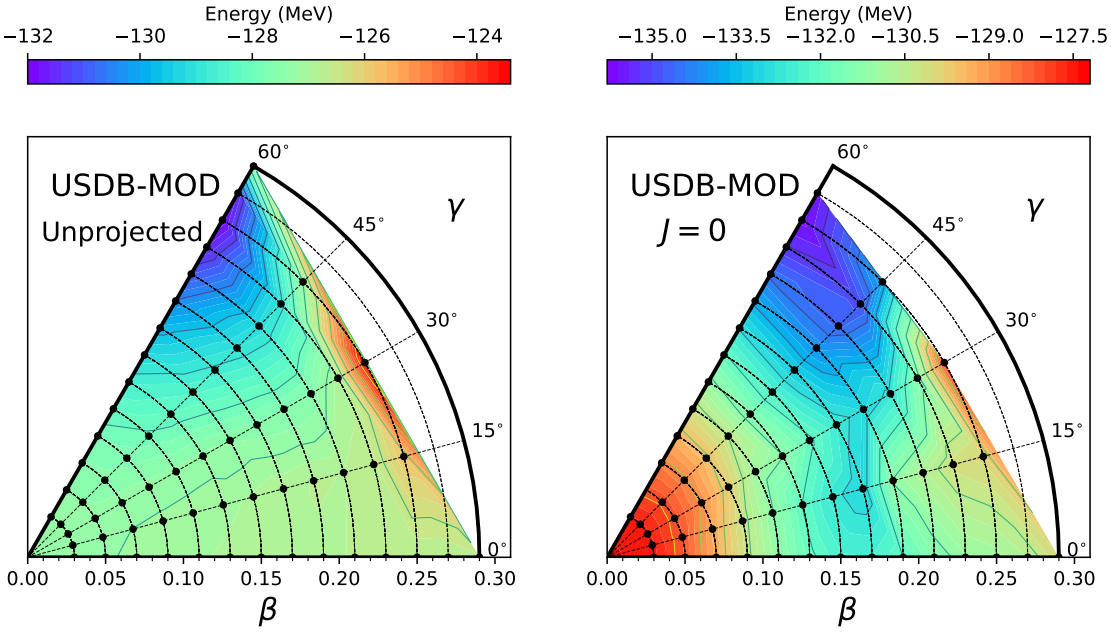

Figure 3.8: Energy surfaces of ^{28}Si using the USDB-MOD interaction for the unprojected (left) and projected to $J = 0$ (right) quadrupole-constrained HFB wavefunctions. Each black circle represents a HFB wavefunction of the mesh.

vergence of the first three 0^+ states is illustrated in Figure 3.9, where the number of natural states included in the basis is varied. I find that the convergence of these states is achieved with the inclusion of up to 47 states from the initial 62 projected HFB states, before encountering any linear dependencies. The convergence pattern observed in USDB-MOD is similar to that of the USDB interaction, demonstrating a favorable agreement with exact diagonalization, as shown in Fig. 3.7.

By computing the GCM states, I am able to determine the collective wavefunctions, which provide insight into the observed enhancement of collectivity indicated by the increased $B(E2)$ transition strengths. In Figure 3.10, the collective wavefunctions of the 0_3^+, 2_2^+, and 4_3^+ states belonging to the normal deformed prolate band are presented. The 0_3^+ bandhead primarily resides in the $\beta \approx 0.3$ region, indicating a larger deformation compared to the USDB result with $\beta \approx 0.23$. Subsequently, the 2_2^+ state mixes with both the $\beta \approx 0.25$ region and incorporates some contribution from the $\beta = 0.17$ minimum. On the other hand, the 4_3^+ state exhibits reduced deformation as it primarily resides in the $\beta = 0.17$ minimum, although it retains a significant component from the $\beta \approx 0.25$ region. Overall, this band demonstrates a progressive decrease in deformation as J increases. However, it is noteworthy that the deformations obtained with the USDB-MOD interaction are larger than those obtained with USDB, and the enhanced transition from 4_3^+ to 2_2^+ is justified within these results. These findings are consistent with the complementary information obtained from the analysis of the USDB-MOD interaction with exact diagonalization. The bottom panel of Fig. 3.6 shows that the 0_3^+ state of the full *sd* shell space acquires nearly double the component of the $|0^+_{\text{4p-4h}}\rangle_{sd}$ fixed configuration. This additional probability is significant and supports the formation of a normal-deformed prolate band, which was not observed with the non-modified USDB interaction.

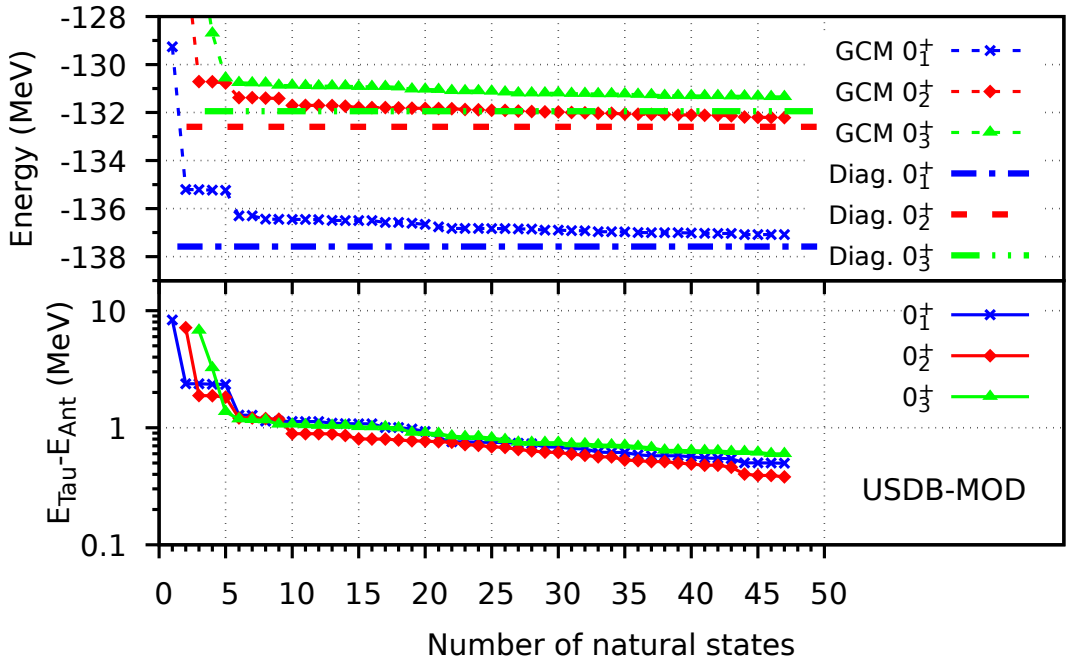

Figure 3.9: (Top panel) Energy evolution of the first three 0^+ states in ^{28}Si with the GCM method as the number of included natural states increases using the USDB-MOD interaction. (Bottom panel) Energy difference between the GCM and exact diagonalization as a function of the number of natural states.

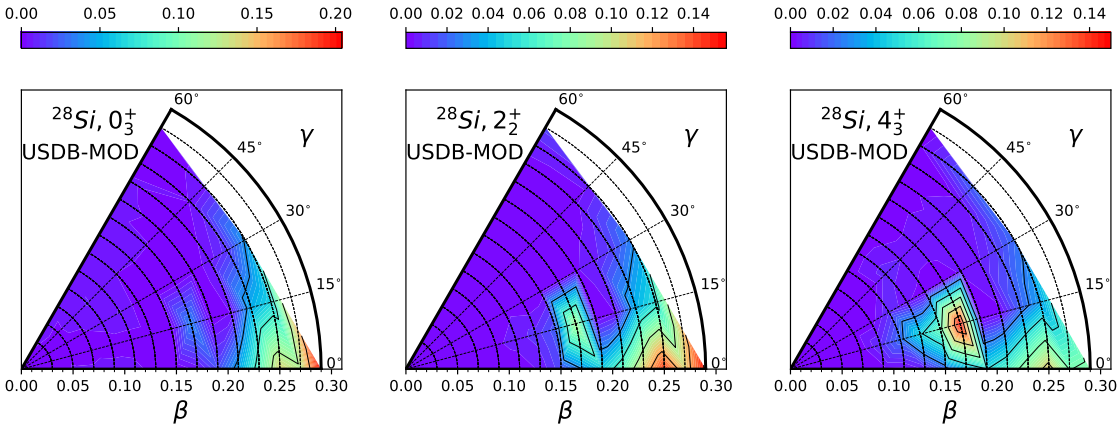

Figure 3.10: Collective wavefunctions of the first three states of the oblate rotational band in ^{28}Si, calculated using the USDB-MOD interaction.

3.3 Superdeformation

In sections 3.1 and 3.2 I have discussed how the oblate rotational band, vibrational band, and prolate rotational band, which exhibit normal deformations, can be effectively described within the *sd* shell. However, the use of this valence space limits on the available deformations among the states of ^{28}Si. Fig. 3.11 shows the deformation parameter value of different np-nh prolate configurations. The analytical $(d_{5/2}$-$s_{1/2}) + d_{3/2}$ prescription reaches a maximum deformation of approximately $\beta \approx 0.3$ at 4p-4h (orange line), which falls short of producing a superdeformed state.

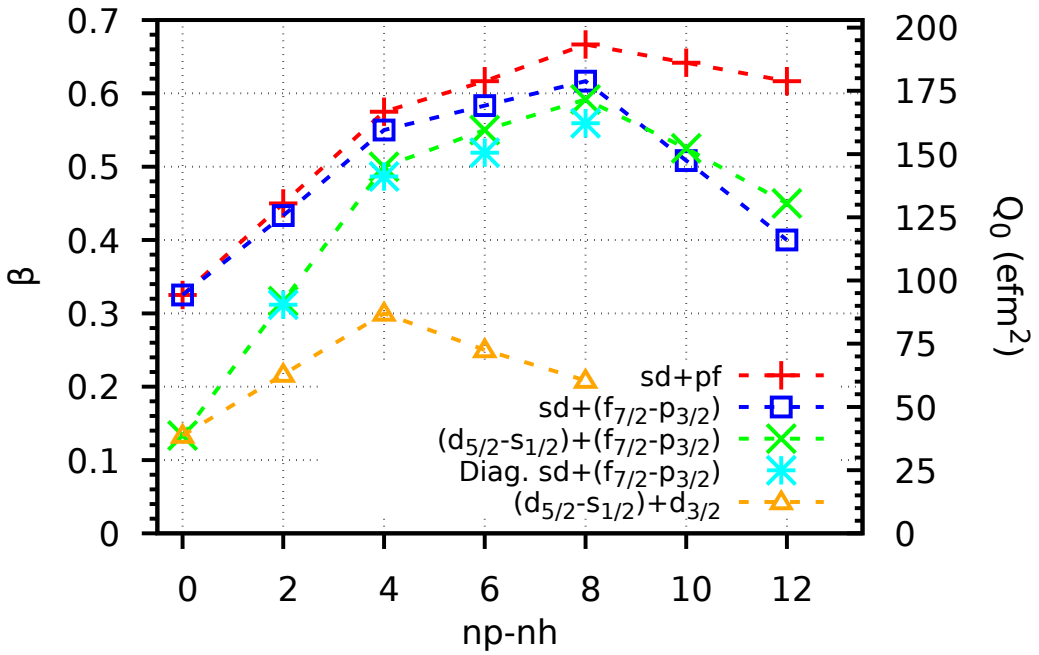

Figure 3.11: Deformation parameters (β) and the intrinsic quadrupole moment (Q_0) for prolate states achieved using different SU(3) variations and numerical calculations.

Therefore, to reach more extreme deformations, the inclusion of orbitals from the pf shell becomes necessary. The formation of superdeformed bands by promotion of particles from the sd shell to the pf shell is a phenomenon that has been found in ^{40}Ca [8], ^{36}Ar [3], ^{40}Ar [13, 14], ^{44}Ti [7] among others, and suggested for ^{28}Si [16] even though it has not been found experimentally despite some recent efforts [19].

We can begin our exploration by considering the SU(3) limit, which encompasses the sd and pf shells. In this limit, all orbits within the same major shell are assumed to have degenerate energies. The deformations resulting from promoting n particles from the sd shell to the pf shell are as follows: $\beta = 0.32, 0.45, 0.57, 0.61, 0.67$ for $n = 0, 2, 4, 6, 8$, as shown by the red crosses in Fig. 3.11. Within this framework, promoting 2 particles is nearly sufficient to reach a superdeformed state. However, it is important to note that the SU(3) limit is not realistic due to the assumption of energy degeneracy among the orbits.

As the previous deformations are overestimated, I seek for a more realistic model that can accurately predict the relevant configurations of np-nh configurations that may form a superdeformed band. Based on my previous analysis of the sd shell, the nearly degenerate doublet of ($d_{5/2}$-$s_{1/2}$) orbitals contributes significantly to the deformation in the sd shell. Considering that promoting particles to the $d_{3/2}$ orbit does not yield sufficient deformation, it is likely that these particles occupy states within the pf shell instead. As a result, the $d_{3/2}$ orbital is expected to contain only a small fraction of particles. The primary source of deformation within the pf shell arises from the quasi-SU(3) orbits, specifically the ($f_{7/2}$-$p_{3/2}$) orbitals. These orbits are closer in energy to the sd shell, as illustrated in Figure 2.1. This observation is further supported by Figure 3.11, where the difference between the blue squares representing the $sd + pf$ shells and the red crosses representing only the sd shell

with the inclusion of ($f_{7/2}$-$p_{3/2}$) orbits is relatively small.

Thus, the key orbits that play a significant role in determining the deformation are the quasi-SU(3) orbits within the *sd* and *pf* shells, forming the $dsfp \equiv$ ($d_{5/2}$-$s_{1/2}$)+($f_{7/2}$-$p_{3/2}$) valence space. The deformations of the np-nh configurations within this space are indicated in green times symbols in Fig. 3.11. Notably, promoting 2 particles to the ($f_{7/2}$-$p_{3/2}$) orbits results in a deformation similar to promoting 4 particles to the $d_{3/2}$ orbit, both yielding a deformation of approximately $\beta \approx 0.3$. The most significant enhancement in deformation, compared to their respective previous configurations, is observed in the 2p-2h and 4p-4h configurations within the ($f_{7/2}$-$p_{3/2}$) orbits, yielding an increase in deformation of approximately $\Delta\beta \approx 0.2$. Considering that the promotion of particles across a major shell incurs a high single-particle energy cost, it is anticipated that the np-nh configurations with $n \geq 6$ will be less relevant, as the marginal increase in deformation, $\Delta\beta \approx 0.05$, is outweighed by the associated energy cost. Therefore, I expect that the superdeformed (SD) state should be composed of the 4p-4h configuration in the *dsfp* space. The 2p-2h configuration cannot be considered a SD shape since its $\beta < 0.5$. Another advantage of the *dsfp* valence space is that, besides capturing the physics of deformation, exact diagonalization is still manageable (dim $\approx 1 \cdot 10^{10}$). In contrast, the complete *sd*+*pf* space is not feasible due to its enormous dimension (dim $\approx 1 \cdot 10^{12}$) resulting from the combinatorial growth of the many-body basis, as described by Eq. (2.26).

Given the change in the valence space from the *sd* shell in Sections 3.1 and 3.2 (using the USDB interaction) to the *sd*+*pf* shells, a different effective interaction is required. However, finding an interaction specifically tailored for ^{28}Si in the $sd+pf$ space proves challenging, as most interactions are either designed for nuclei with a filled $d_{5/2}$ orbit or assume a neutron-rich composition. Consequently, I have opted to employ the SDPF-NR interaction [52], which was developed for neutron-rich silicon isotopes such as ^{34,35}Si.

In the $sd+pf$ space, the single-particle energies of the orbits are given in Table 3.2. Notably, there is a substantial energy gap between the $d_{3/2}$ and $f_{7/2}$ orbits, indicative of a major shell closure. Additionally, the $f_{7/2}$, $p_{3/2}$, and $f_{5/2}$ orbits are nearly degenerate in energy. To perform the calculations, I reduce the space from *sd*+*pf* to *sd*+($f_{7/2}$-$p_{3/2}$) for the exact diagonalization. Excluding the $p_{1/2}$ orbit is justified due to its energy being approximately 4 MeV higher than the rest of the *pf* shell orbits. Moreover, the $f_{5/2}$ orbit can be neglected since, for quadrupole properties, the dominant contribution arises from the quasi-SU(3) $f_{7/2}$-$p_{3/2}$ orbits.

The deformations associated with the np-nh configurations in the *sd*+($f_{7/2}$-$p_{3/2}$) valence space are shown in Fig. 3.11 in cyan asterisks. The agreement with the *dsfp* scheme, in green times symbols, is noticeable, even though the exact diagonalization includes the $d_{3/2}$ orbit. This supports that the 4p-4h configuration provides the best candidate for the formation of a superdeformed state.

Table 3.2: Single-particle energies (SPE) of the orbits in the $sd+pf$ space for the SDPF and SDPF-4MeV interactions. The SPE of the *sd*-shell orbits correspond to those of the USDB interaction.

SPE	$d_{5/2}$	$s_{1/2}$	$d_{3/2}$	$f_{7/2}$	$p_{3/2}$	$f_{5/2}$	$p_{1/2}$
SDPF-NR (MeV)	-3.699	-2.915	1.895	6.220	6.314	6.479	10.950
SDPF-4MeV (MeV)	-3.699	-2.915	1.895	2.220	2.314	2.479	6.950

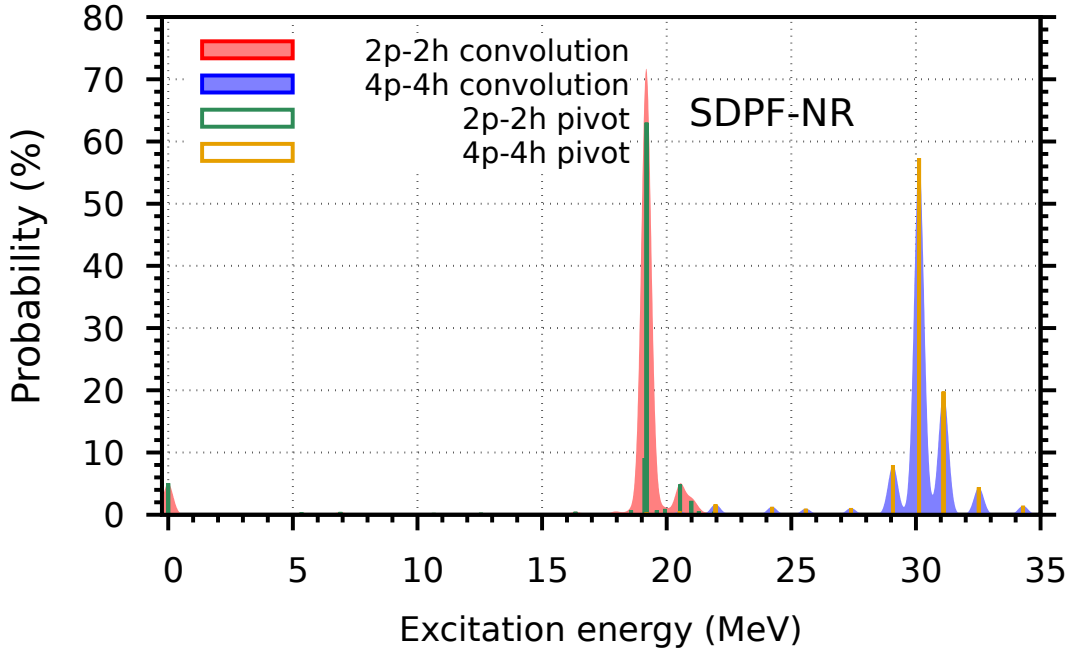

Figure 3.12: Probability (%) of finding the lowest energy state with fixed 2p-2h and 4p-4h configuration in the full sd+($f_{7/2}$-$p_{3/2}$) states $|0^+_\sigma\rangle_{sdfp}$ with the SDPF-NR interaction. Each eigenstate is convoluted with Gaussians of 200 keV width.

Following the same strategy as in Section 3.2, we can use the np-nh configurations as a pivot state to perform an exact diagonalization in the full $sd+(f_{7/2}$-$p_{3/2})$ space

$$|0^+_{n\text{p-}n\text{h}}\rangle_{sdfp} = \frac{1}{N}\sum_\sigma S(\sigma)|0^+_\sigma\rangle_{sdfp}. \tag{3.2}$$

Figure 3.12 illustrates the Lanczos strength function of the 2p-2h and 4p-4h configurations using the SDPF-NR interaction. The former primarily resides at an excitation energy of approximately 19 MeV, while the latter exhibits some fragmentation in the region around 30 MeV, with a width of 1 MeV.

The approximate single-particle cost of promoting these particles can be estimated by considering the gap between the $d_{3/2}$ and $f_{7/2}$ (or $p_{3/2}$) orbits, which is almost 10 MeV. For the 2p-2h configuration, the excitation energy is nearly 2 times this value, approximately 19 MeV. Meanwhile, for the 4p-4h configuration, the excitation energy lies around 10 MeV lower than expected, which can be attributed to the increased quadrupole correlations resulting from its high deformation. However, it is important to remark that due to its significantly higher energy, the Lanczos strength function for the 4p-4h configuration is not fully converged in energy.

Then, if the SD band is dominated solely from a pure np-nh configuration, my calculations predict that the 2p-2h configuration would appear at 19 MeV, and the 4p-4h configuration at 30 MeV in my calculations. However, this result is in contrast with the findings of the study on superdeformation in ^{28}Si [19], where a structure with 4 particles promoted to the pf-shell yields a superdeformed bandhead at 13 MeV ($\beta \approx 0.6$). The 4p-4h structure I find is less deformed ($\beta \approx 0.5$) and lies much higher in energy than the one found in the aforementioned study.

In order to identify a superdeformed state within the full sd+($f_{7/2}$-$p_{3/2}$) space, it would be necessary to compute the $|0^+_\sigma\rangle_{sdfp}$ states as well as the $|2^+_\sigma\rangle_{sdfp}$ states,

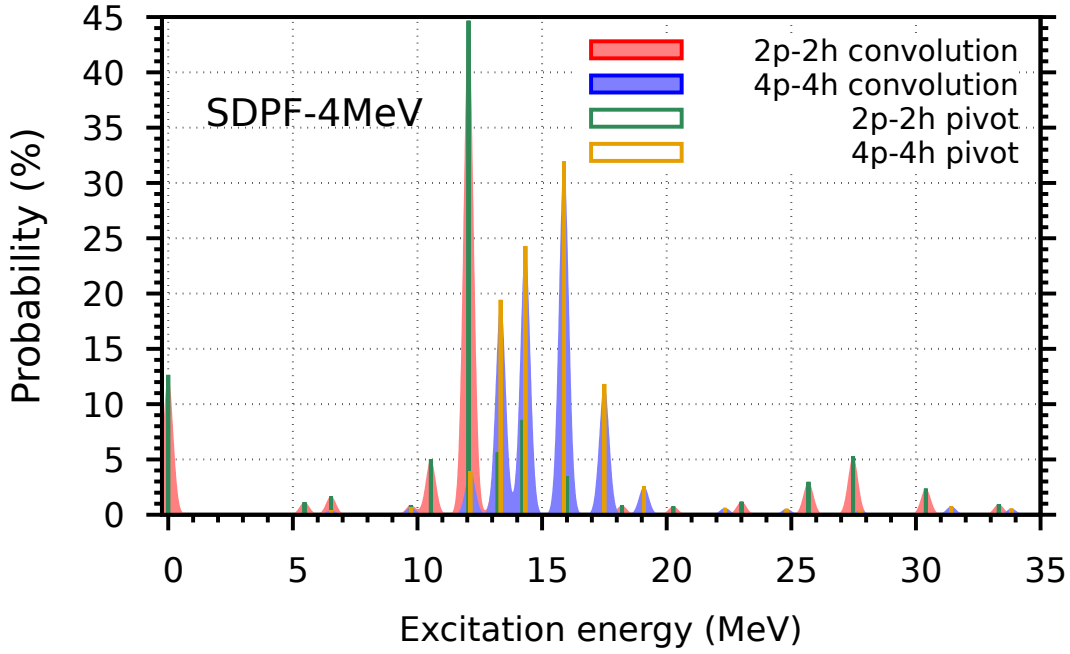

Figure 3.13: Probability (%) of finding the lowest energy state with fixed 2p-2h and 4p-4h configuration in the full sd+($f_{7/2}$-$p_{3/2}$) states $|0^+_\sigma\rangle_{sdfp}$ with the SDPF-4MeV interaction. Each eigenstate is convoluted with Gaussians of 200 keV width.

since they are required for calculating the $B(E2)$ transitions and the spectroscopic quadrupole moments Q_{spec}. However, considering an energy of $E_{\text{exc}} \leq 15$ MeV, this would involve calculating fully converged states with $\sigma \simeq 10$ for both J^+_σ. This calculation is extremely computationally demanding within such space. Therefore, an alternative approach is needed.

The variational approach proves to be more convenient in this case. Once the projection onto good quantum numbers of the HFB states is performed, which is computationally the most demanding step, the solution of the HWG equation (2.51) enables the computation of any $|0^+_\sigma\rangle$ state. Computing these states is enough to locate the SD states, as we can identify the SD states with the collective wavefunctions. However, as σ increases, the variational approach provides a poorer approximation to the exact diagonalization. To address this limitation, it is helpful to artificially modify the interaction such that higher deformation states appear at lower energies in the spectrum. This can be achieved by reducing the single-particle energies of the pf-shell orbits. The modification I employ, referred to as SDPF-4MeV, is presented in Table 3.2. The chosen adjustment in single-particle energies corresponds to a reduction of 4 MeV, which is the maximum energy that maintains the pf shell above the sd-shell orbits without altering them. However, since the modification strongly favors states with pf-shell excitations, these configurations may mix with lower energy states. Figure 3.13 displays the strength functions, Eq. (3.2), of the same 2p-2h and 4p-4h configurations using the SDPF-4MeV interaction. With this modification, the gap between the $d_{5/2}$ and $f_{7/2}$ decreases from approximately 10 MeV to 6 MeV. Consequently, the 2p-2h configuration shifts from 19 MeV to 12 MeV, and the 4p-4h configuration moves from 30 MeV to 15 MeV, albeit fragmenting among several states. Additionally, the 2p-2h configuration also contributes to the ground

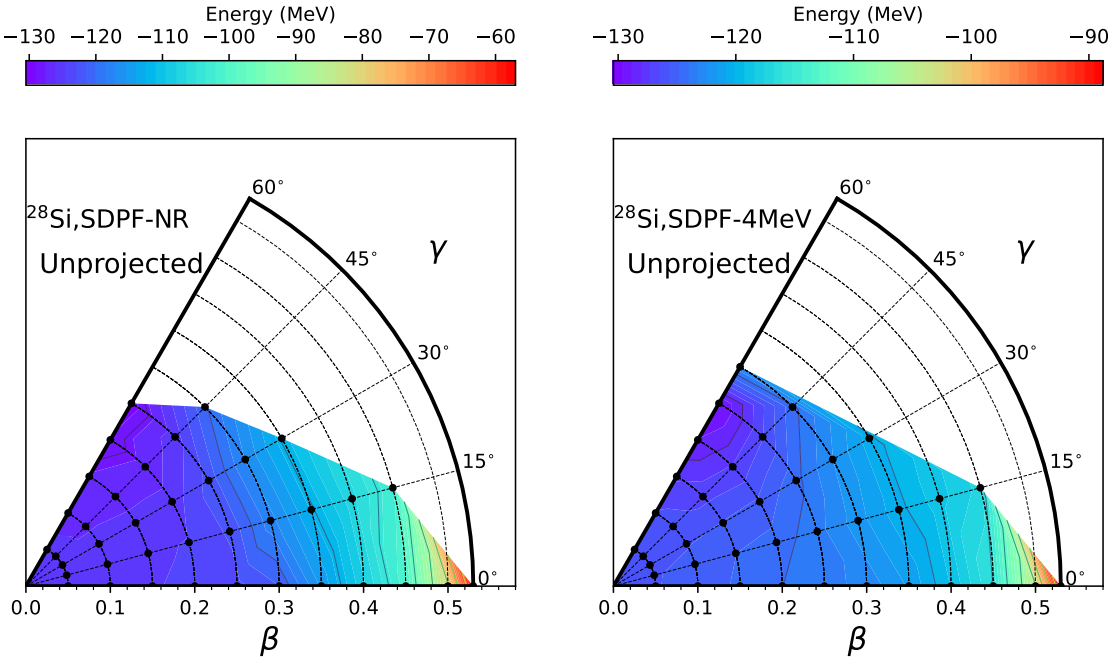

Figure 3.14: Energy surfaces of ^{28}Si using the SDPF-NR (left) and the SDPF-4MeV (right) interaction for the unprojected quadrupole-constrained HFB wavefunctions. Each black circle represents a HFB wavefunction of the mesh.

state due to the artificial energy modification I have introduced. Nevertheless, the results are consistent with the ones from the non-modified SDPF-NR interaction. These results suggest that the SD structure does not survive configuration mixing. In particular, the analysis strongly disfavors the appearance of the SD band below 15 MeV.

We can also examine the impact of the SDPF-NR and SDPF-4MeV interactions on the unprojected HFB surfaces in the sd+($f_{7/2}$-$p_{3/2}$) space, as shown in Figure 3.14. Both panels show that the absolute minimum remains in the oblate region with a deformation of approximately $\beta \approx -0.25$, which is consistent with the results obtained using the USDB interaction shown in Figure 3.1. This indicates that the inclusion of pf-shell orbits does not significantly alter the physics of the previously described states within the sd shell. However, the addition of pf-shell orbits enables higher deformations in the prolate region, from approximately $\beta \approx 0.3$ to $\beta \approx 0.5$. These results support the capability of the SDPF-NR interaction to accommodate highly deformed states using the SDPF-NR and SDPF-4MeV interactions. The only difference is that the modified SDPF-4MeV interaction shows a smaller energy range between the minimum and maximum values compared to the original SDPF-NR interaction. This reduction in range is a result of the decreased single-particle energy required to promote particles to the pf shell.

By performing projection onto good quantum numbers and employing the GCM method to mix the states, I can examine the collective wavefunctions of the SD states in the sd+($f_{7/2}$-$p_{3/2}$) space using the SDPF-4MeV interaction. Figure 3.15 highlights the notable prolate structures in the spectrum. Starting with the 0^+_3 state at an excitation energy of $E_{\rm ex} = 7.22$ MeV, this state exhibits a moderate deformation with $\beta \approx 0.3$, similar to the prolate bandhead obtained with the USDB-

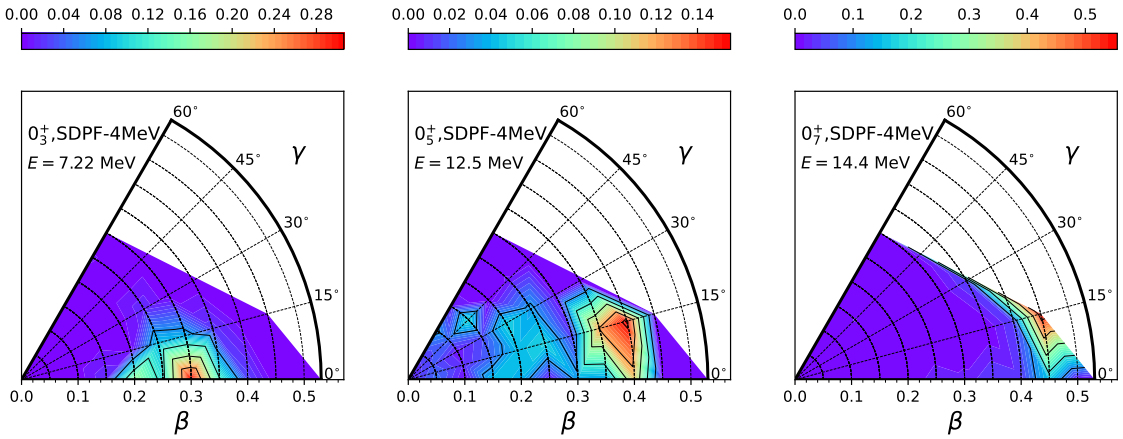

Figure 3.15: Collective wavefunctions of selected 0^+ states with prolate deformation in ^{28}Si in the sd+($f_{7/2}$-$p_{3/2}$) space, calculated using the SDPF-4MeV interaction.

MOD interaction in Figure 3.10. Furthermore, this state is predominantly contained within the sd shell, with only a fraction of 0.5 out of 12 particles promoted to the pf-shell orbits. This suggests that it corresponds to the equivalent of the ND prolate bandhead from USDB using the SDPF-4MeV or SDPF-NR interaction, as the pf-shell orbits play a negligible role in this state. Although not shown, the 0_1^+ and 0_2^+ states can also be associated with their respective USDB counterparts for the oblate and vibrational bandheads based on their deformations and occupation patterns. This provides further evidence that the SDPF-NR or SDPF-4MeV interaction is well-suited to describe ^{28}Si.

The lowest energy state exhibiting significant deformations is the 0_5^+ state at 12.5 MeV, predominantly composed of the $\beta = 0.4$ and $\gamma = 0.15°$ projected HFB state. The occupation numbers of pf-shell orbits in this particular HFB state are approximately $n_{f_{7/2}} \approx 2$ and $n_{p_{3/2}} \approx 1$, totaling 3 particles in the pf shell. Likewise, the 0_7^+ state at 14.4 MeV displays a deformation of $\beta = 0.45$ and $\gamma = 0.15°$, with 4 particles occupying the pf-shell. Although these states may exhibit properties resembling SD states in ^{28}Si, it is important to consider the impact of the modified interaction used. The states obtained with the SDPF-4MeV interaction already appear at 12.5 and 14.4 MeV, falling within the energy range expected for SD states in ^{28}Si according to previous studies [16]. However, if we naively add the single-particle energy cost of 4 MeV/particle due to the reduced $d_{5/2}$-$f_{7/2}$ gap in the SFPF-4MeV interaction, compared to the original SDPF-NR one, the 0_5^+ state would be placed at 24 MeV and the 0_7^+ state at 28.5 MeV. This supposition is merely qualitative, as the states obtained through configuration mixing would differ, since the energy of the projected HFB states in the high deformation region would be higher and thus less favorable on average. Therefore, according to my calculations, it appears unlikely that a low-lying SD state exists in ^{28}Si within the energy range of $E_{\text{ex}} \lesssim 15$ MeV. Instead, a more realistic view is to suppose that the configurations with particles in the pf shell mix with less deformed states of the sd shell, as suggested by the fragmentation in Fig. 3.13, and the mixed sd-pf nature of the 0_5^+ state in Fig. 3.15.

Finally, I have performed a GCM calculation in the full $sdpf$ space, considering all orbits of the sd and pf shells. This calculation is only possible within the

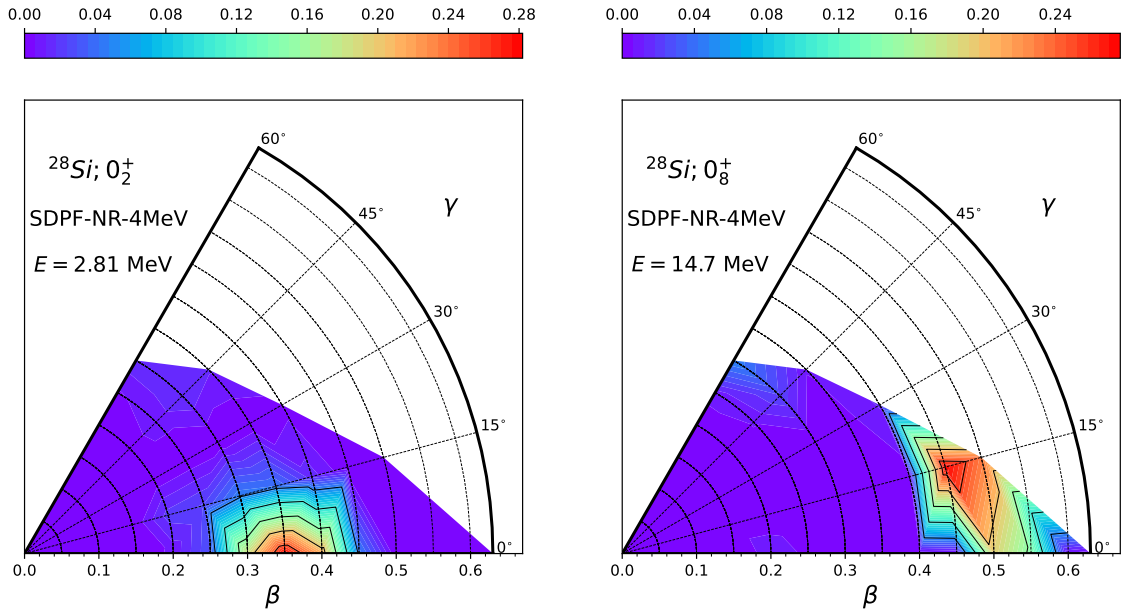

Figure 3.16: Collective wavefunctions of selected prolate states in the full $sdpf$ space using the SDPF-4MeV interaction.

variational approach, as the exact diagonalization is unfeasible. With the inclusion of the additional pf-shell orbits, the deformations that can be reached increase from $\beta \approx 0.5$ to $\beta \approx 0.6$. This observation aligns with my previous analysis of Fig. 3.11, as the predominant source of deformation in the pf shell arises from its quasi-SU(3) orbits.

Figure 3.16 presents the collective wavefunctions of the 0_2^+ state at 2.8 MeV and the 0_8^+ state at 15 MeV. The 0_2^+ state exhibits a deformation of approximately $\beta \approx 0.35$ at an unusually low energy of only 2.8 MeV. The corresponding projected HFB state with $\beta \approx 0.35$ contains 3 particles distributed among the pf-shell orbits. This state is likely an artifact arising from the modification of the interaction. Because the single-particle energy cost of pf shell excitations is greatly reduced, this state captures additional correlations that brings it too low in energy, compared to any experimental state. When searching for a genuine superdeformed (SD) state, the 0_8^+ state at 15 MeV emerges as the only candidate. It exhibits a deformation characterized by $\beta = 0.45$ and $\gamma = 0.15°$. However, a similar issue arises as observed in the analysis of the sd+($f_{7/2}$-$p_{3/2}$) space. The energy at which the 0_8^+ state appears is too high to be considered as a candidate for the formation of low-lying SD states in ^{28}Si.

In sum, the results obtained from the fixed np-nh calculation indicate that the formation of superdeformed (SD) structures solely from pure np-nh configurations extending to the pf shell is unlikely in the $10 - 15$ MeV energy region. This conclusion is further supported by the GCM calculations, which also show no evidence of such SD structures at low energy. Due to the significant energy cost associated with promoting particles to the pf-shell, it is more likely that the mixing of these states with normal-deformed configurations would give rise to moderately deformed states within the the 10-15 MeV energy range rather than SD states.

4. Conclusions and Outlook

In this study, I focus on investigating shape coexistence in the nucleus ^{28}Si. The oblate rotational band and its corresponding vibration is successfully reproduced by diagonalizing the effective USDB interaction within a valence space consisting of the *sd* shell. Two methods, exact diagonalization and a variational approach, are employed yielding excellent agreement not only with each other but also with experimental data.

However, the rotational prolate band is not accurately reproduced with the USDB interaction. Guided by Elliott's SU(3)-variants, I find that the promotion of four particles from the $d_{5/2}$-$s_{1/2}$ nearly-degenerated orbits to the $d_{3/2}$ orbit is compatible with the experimental prolate band. Therefore, I introduce a reduction in the single-particle energy of the $d_{3/2}$ orbit, denoted as USDB-MOD, to favor this configuration. With the implementation of the USDB-MOD effective interaction, a rotational prolate band in agreement with the experimental data is obtained, while the band structure of the oblate rotational and vibrational bands is preserved.

The work also examines the potential formation of superdeformed structures at higher energies. According to Elliott's SU(3) schemes, it is established that the inclusion of the pf shell is necessary to achieve highly deformed states with $\beta \geq 0.3$. The primary contributions to deformation originate from the quasi-SU(3) orbits of the pf-shell, the $f_{7/2}$ and $p_{3/2}$ orbits. Considering the significant energy required to promote particles to the pf shell, it is concluded that the 4p-4h configuration, with $\beta \approx 0.5$, is the most promising candidate for a superdeformed structure. Previous studies have suggested the existence of superdeformed (SD) states in the energy range of 10-15 MeV. However, my calculations using the exact diagonalization of the SDPF-NR interaction for fixed np-nh configurations show that the 2p-2h and 4p-4h states are located at approximately 20 and 30 MeV, respectively. The 4p-4h state also exhibits fragmentation among the states in the full sd+($f_{7/2}$-$p_{3/2}$) space. Although the variational approach reveals potential almost superdeformed structures, their excitation energies are also too high. Consequently, the numerical calculations in this study suggest that the superdeformed state would mix with normal-deformed configurations. My results strongly disfavor that ^{28}Si exhibits a distinct superdeformed band.

This study suggests several avenues for future research. Firstly, for the low-lying states of ^{28}Si, a more sophisticated modification of the USDB interaction can be considered, focusing on adjusting the monopoles, the part of the two-body interaction related to the effective evolution of the single-particle energies, instead of solely modifying the single-particle energy of the $d_{3/2}$ orbit. This approach may lead to a more precise description of the coexisting band structures observed in the nucleus. Additionally, the investigation of the hexadecapole moment of the ground state, as recently measured [53], presents an opportunity for further exploration, testing the theoretical predictions. Examining this observable can provide deeper insights into

the nuclear structure of ^{28}Si. Regarding the superdeformed (SD) states, a thorough analysis can be conducted by diagonalizing the non-modified SDPF-NR interaction. This would enable a more comprehensive understanding of the configuration mixing between the normal-deformed and superdeformed states.

These avenues of research have the potential to enhance our understanding of nuclear structure and provide valuable insights into the properties of ^{28}Si and other nuclei. For instance, the analysis employed in this study can be extended to other nuclei, particularly those that have been proposed to exhibit superdeformed structures, such as ^{32}S. An extensive analysis similar to that conducted for ^{28}Si can be carried out for these nuclei, providing valuable insight into their nuclear properties and the possible presence of superdeformation driven by nucleons in the sd and pf shells.

Bibliography

1. Garrett, P. E., Zielińska, M. & Clément, E. An experimental view on shape coexistence in nuclei. *Progress in Particle and Nuclear Physics* **124,** 103931 (2022).
2. Itoh, M. *et al.* Isoscalar giant resonance strengths in ^{32}S and possible excitation of superdeformed and ^{28}Si+α cluster bandheads. *Physical Review C* **88,** 064313 (2013).
3. Svensson, C. *et al.* Superdeformation in the N=Z Nucleus ^{36}Ar: Experimental, Deformed Mean Field, and Spherical Shell Model descriptions. *Physical Review Letters* **85,** 2693 (2000).
4. Ideguchi, E. *et al.* Superdeformation in asymmetric N>Z nucleus ^{40}Ar. *Physics Letters B* **686,** 18 (2010).
5. Middleton, R., Garrett, J. & Fortune, H. Search for multiparticle-multihole states of ^{40}Ca with the ^{32}S (^{12}C, α) reaction. *Physics Letters B* **39,** 339 (1972).
6. Napiorkowski, P. *et al.* Superdeformed and Triaxial States in ^{42}Ca. *Physical Review Letters* **117,** 062501 (2016).
7. O'Leary, C. *et al.* Nonyrast high-spin states in N=Z ^{44}Ti. *Physical Review C* **61,** 064314 (2000).
8. Caurier, E., Menéndez, J., Nowacki, F. & Poves, A. Coexistence of spherical states with deformed and superdeformed bands in doubly magic ^{40}Ca: A shell-model challenge. *Physical Review C* **75,** 054317 (2007).
9. Dowie, J. *et al.* Evidence for shape coexistence and superdeformation in ^{24}Mg. *Physics Letters B* **811,** 135855 (2020).
10. Jenkins, D. *et al.* Candidate superdeformed band in ^{28}Si. *Physical Review C* **86,** 064308 (2012).
11. Kubono, S. *et al.* Highly excited high spin states in ^{28}Si populated through the ^{12}C (^{20}Ne, α) reaction. *Nuclear Physics A* **457,** 461 (1986).
12. Rodríguez-Guzmán, R., Egido, J. & Robledo, L. Properties of the predicted superdeformed band in ^{32}S. *Physical Review C* **62,** 054308 (2000).
13. Taniguchi, Y. *et al.* Triaxial superdeformation in ^{40}Ar. *Physical Review C* **82,** 011302 (2010).
14. Yang, Y.-C., Liu, Y.-X., Sun, Y. & Guidry, M. Superdeformed band in the N=Z+4 nucleus ^{40}Ar: A projected shell model analysis. *The European Physical Journal A* **54,** 1 (2018).
15. Endt, P. Supplement to energy levels of A= 21–44 nuclei (VII). *Nuclear Physics A* **633,** 1 (1998).
16. Taniguchi, Y., Kanada-En'yo, Y. & Kimura, M. Cluster structures and superdefomation in ^{28}Si. *Physical Review C* **80,** 044316 (2009).
17. Mayer, M. G. On closed shells in nuclei. II. *Physical Review* **75,** 1969 (1949).
18. Haxel, O., Jensen, J. H. D. & Suess, H. E. On the "magic numbers" in nuclear structure. *Physical Review* **75,** 1766 (1949).

19. Morris, L. *et al.* Search for in-band transitions in the candidate superdeformed band in ^{28}Si. *Physical Review C* **104,** 054323 (2021).

20. Greiner, W., Maruhn, J. A., *et al. Nuclear models* (Springer, 1996).

21. Bally, B., Sánchez-Fernández, A. & Rodríguez, T. R. Symmetry-projected variational calculations with the numerical suite TAURUS: I. Variation after particle-number projection. *The European Physical Journal A* **57,** 1 (2021).

22. Suhonen, J. *From nucleons to nucleus: concepts of microscopic nuclear theory* (Springer Science & Business Media, 2007).

23. Blomqvist, J. & Molinari, A. Collective 0^- vibrations in even spherical nuclei with tensor forces. *Nuclear Physics A* **106,** 545 (1968).

24. Fortunato, L. Solutions of the Bohr Hamiltonian, a compendium. *The European Physical Journal A* **26,** 1 (2005).

25. Varshalovich, D. A., Moskalev, A. N. & Khersonskii, V. K. *Quantum theory of angular momentum* (World Scientific, 1988).

26. Poves, A. & Nowacki, F. in *An Advanced Course in Modern Nuclear Physics* 70 (Springer, 2001).

27. Hebeler, K. Three-nucleon forces: Implementation and applications to atomic nuclei and dense matter. *Physics Reports* **890,** 1 (2021).

28. Agostini, M., Benato, G., Detwiler, J. A., Menéndez, J. & Vissani, F. Toward the discovery of matter creation with neutrinoless $\beta\beta$ decay. *Reviews of Modern Physics* **95,** 025002 (2023).

29. Engel, J. & Menéndez, J. Status and future of nuclear matrix elements for neutrinoless double-beta decay: a review. *Reports on Progress in Physics* **80,** 046301 (2017).

30. Hagen, G., Papenbrock, T., Hjorth-Jensen, M. & Dean, D. J. Coupled-cluster computations of atomic nuclei. *Reports on Progress in Physics* **77,** 096302 (2014).

31. Hergert, H., Bogner, S., Morris, T., Schwenk, A. & Tsukiyama, K. The in-medium similarity renormalization group: A novel ab initio method for nuclei. *Physics reports* **621,** 165 (2016).

32. Carlson, J. *et al.* Quantum Monte Carlo methods for nuclear physics. *Reviews of Modern Physics* **87,** 1067 (2015).

33. Barrett, B. R., Navrátil, P. & Vary, J. P. Ab initio no core shell model. *Progress in Particle and Nuclear Physics* **69,** 131 (2013).

34. Navrátil, P., Quaglioni, S., Hupin, G., Romero-Redondo, C. & Calci, A. Unified ab initio approaches to nuclear structure and reactions. *Physica Scripta* **91,** 053002 (2016).

35. Elliott, J. P. Collective motion in the nuclear shell model. I. Classification schemes for states of mixed configurations. *Proceedings of the Royal Society of London. Series A. Mathematical and Physical Sciences* **245,** 128 (1958).

36. Talmi, I. *Simple models of complex nuclei* (Routledge, 2017).

37. Retamosa, J., Udias, J., Poves, A. & De Guerra, E. M. 1^+ Excitations in light nuclei: SU(3) versus realistic shell model results. *Nuclear Physics A* **511,** 221 (1990).

38. Richter, W., Mkhize, S. & Brown, B. A. sd-shell observables for the USDA and USDB Hamiltonians. *Physical Review C* **78,** 064302 (2008).

39. Brown, B. A. & Richter, W. New "USD" Hamiltonians for the sd shell. *Physical Review C* **74,** 034315 (2006).

40. Zuker, A., Poves, A., Nowacki, F. & Lenzi, S. Nilsson-SU(3) self-consistency in heavy N=Z nuclei. *Physical Review C* **92,** 024320 (2015).

41. Zuker, A., Retamosa, J., Poves, A. & Caurier, E. Spherical shell model description of rotational motion. *Physical Review C* **52,** R1741 (1995).

42. Shimizu, N., Mizusaki, T., Utsuno, Y. & Tsunoda, Y. Thick-restart block Lanczos method for large-scale shell-model calculations. *Computer Physics Communications* **244,** 372 (2019).

43. Caurier, E. *et al.* Shell model code ANTOINE. *IReS, Strasbourg* **2002** (1989).

44. Caurier, E. Shell model code ANTOINE 1989-2004; E. Caurier and F. Nowacki. *Acta. Phys. Pol* **30,** 2 (1999).

45. Caurier, E., Martínez-Pinedo, G., Nowacki, F., Poves, A. & Zuker, A. The shell model as a unified view of nuclear structure. *Reviews of Modern Physics* **77,** 427 (2005).

46. Dao, D. & Nowacki, F. Nuclear structure within a discrete nonorthogonal shell model approach: New frontiers. *Physical Review C* **105,** 054314 (2022).

47. Fernández, A. S. *Implementación del método de la coordenada generadora con interacciones nucleares genéricas: El proyecto Taurus.* PhD thesis (Universidad Autónoma de Madrid, 2022).

48. Griffiths, D. J. & Schroeter, D. F. *Introduction to quantum mechanics* (Cambridge university press, 2018).

49. Ring, P. & Schuck, P. *The nuclear many-body problem* (Springer Science & Business Media, 2004).

50. Martínez-Larraz, J. & Rodríguez, T. R. Optimization of the number of intrinsic states included in the discrete generator coordinate method. *Physical Review C* **106,** 054301 (2022).

51. Sheikh, J. A., Dobaczewski, J., Ring, P., Robledo, L. M. & Yannouleas, C. Symmetry restoration in mean-field approaches. *Journal of Physics G: Nuclear and Particle Physics* **48,** 123001 (2021).

52. Nummela, S. *et al.* Spectroscopy of ^{34,35}Si by β decay: sd-fp shell gap and single-particle states. *Physical Review C* **63,** 044316 (2001).

53. Gupta, Y. *et al.* Precise determination of quadrupole and hexadecapole deformation parameters of the *sd*-shell nucleus, ^{28}Si. *arXiv: 2303.12495* (2023).